Quart. J. R. Met. Soc. (1979), **105**, pp. 915–944

551.506.5(729.86): 551.509.313:551.511.61

A numerical simulation of BOMEX data using a turbulence closure model coupled with ensemble cloud relations

By TETSUJI YAMADA and GEORGE L. MELLOR

Radiological and Environmental Research Division, Argonne National Laboratory, Argonne, Ill. 60439

Geophysical Fluid Dynamics Program, Princeton University, Princeton, N.J. 08540

(Received 1 August 1978; revised 6 March 1979)

Summary

A one-dimensional version of a simplified second-moment turbulence closure model, coupled with a recently developed cloud model, is used to simulate BOMEX (Barbados Oceanographic and Meteorological Experiment) data. Partial differential equations for the turbulence energy and a master length scale are solved. Simulated mixing ratios of water vapour, virtual temperatures and horizontal wind speeds are compared with observations. Horizontal wind speeds agree quite well; however, simulated temperature and mixing ratio of water vapour at the end of the fourth day are about 2 K and 1·5 g kg^{-1} higher, respectively, than corresponding observations; possibly this is due to the fact that the surface temperature used in the simulation is too high. Mean liquid water, cloud volume, liquid water variance, turbulence energy and eddy viscosity coefficients are presented, but data for these variables are not available for comparison. Surface momentum, heat and moisture fluxes are also presented and are compared with data. Sensitivity studies indicate that the simulated mixing ratios of water vapour agree best with observations when both vertical wind and horizontal advection obtained from the data are included.

The present study is encouraging, although further research is required to improve the model and to develop confidence in its predictive capability.

1. Introduction

As reviewed by Mellor and Yamada (1977) a second-moment turbulence closure model has demonstrated considerable skill in simulating various turbulent flows encountered in laboratory experiments and in atmospheric and oceanic boundary layers. Other studies using similar closure models have been reported (Lewellen *et al.* 1974; Wyngaard and Coté 1974; Lumley and Khajeh-Nouri 1974; Zeman and Lumley 1976; Burk 1977). A second-moment closure turbulence model has been also used to model 'subgrid-scale turbulence' in fully three-dimensional and unsteady flow simulations (Deardorff 1974a,b; Sommeria 1976). Even more complex, a third-moment turbulence closure model has been developed (André *et al.* 1976a,b, 1978). Such approaches are attractive compared with the more conventional eddy viscosity methods since they incorporate a more realistic physical description of turbulence than the latter and, as will be demonstrated here, can be extended to include more complex situations where temperature, water vapour and liquid water are all important. Adequate formulation of an eddy viscosity becomes virtually impossible under such conditions. On the other hand, a disadvantage of the full second-moment closure model is its complexity relative to the eddy viscosity models. Thus, from an order-of-magnitude analysis based on a parameter representing the deviation from isotropy (Mellor and Yamada 1974) and experience derived from numerical simulations, a 'model of compromise' has been proposed (Yamada and Mellor 1975). This model, referred to as a level 2·5 model*, requires the solution of differential equations for only turbulence energy and turbulence length scale, the rest of the second-moment equations being reduced to a set of algebraic equations in which tendency, advection and diffusion terms are omitted.

* 'Level' indicates the level of model complexity as defined in Mellor and Yamada. The most complex model there is referred to as a level 4 model.

Although greatly simplified, the level 2·5 model retains most of the essential features of the full closure model. As described and tested by Yamada (1977) in a simulation of the Wangara data (Clarke *et al.* 1971), the level 2·5 model produced results that compared favourably with results from a higher-level model utilized by Yamada and Mellor (1975). The level 2·5 model has also been incorporated in a general circulation model by Miyakoda and Sirutis (1977) to obtain significant improvement over their previous parametrization. For example, the model ran successfully without the dry convective adjustment model (instantaneous mixing to eliminate instability) and eliminated physically unrealistic surface cooling previously associated with that model.

This study demonstrates the capability of a level 2·5 model to simulate the planetary boundary layer over tropical oceans, where water vapour and the condensation process play significant roles in determining boundary layer dynamics. The ensemble cloud relations proposed recently (Sommeria and Deardorff 1977; Mellor 1977) are here incorporated into the level 2·5 model with the aim of simulating BOMEX (Barbados Oceanographic and Meteorological Experiment) data (Holland and Rasmusson 1973). The BOMEX project, which was conducted over and in the tropical ocean near Barbados (Fig. 1), generated considerable data which have been extensively analysed.* The experiment was performed in four intervals: here, period III (22–29 June 1969) is examined since it is the only period when upper air soundings were made; however, surface layer data were not collected during this period. The first part of period III (22–26 June) was characterized as an undisturbed period; the second half was referred to as disturbed. Whether the atmosphere was disturbed or not was determined on the basis of several factors, including the synoptic situation, cloud activity and the amount of precipitation (Nitta and Esbensen 1974). Since a one-dimensional model will be used here for simplicity, the present study is limited to the undisturbed period (little cumulus activity, subsidence predominant, little precipitation).

In the following section a full description of the level 2·5 model, including a cloud model based on a Gaussian probability function, is presented. Then a one-dimensional version of the model is used to simulate the BOMEX data and the results are discussed and compared with the data.

2. Description of the model

In the following developments, upper case letters with tildes represent instantaneous quantities; upper case letters alone are ensemble mean quantities; thus, for example, $\tilde{U} = U$. Fluctuating quantities are represented by lower case letters; so, $\tilde{U} = U+u$ and $\bar{u} = 0$. An exception is density, where ρ is the mean density. A list of symbols is given in appendix B.

(a) *Condensation dynamics*

The conservation equations for the mixing ratios† of water vapour and liquid water are

$$\tilde{D}\tilde{Q}_v/Dt = \eta_v \partial^2 \tilde{Q}_v/\partial x_k^2 - \tilde{\sigma}_c \quad . \quad . \quad . \quad (1)$$

and

$$\tilde{D}\tilde{Q}_l/Dt = \eta_l \partial^2 \tilde{Q}_l/\partial x_k^2 + \tilde{\sigma}_c, \quad . \quad . \quad . \quad (2)$$

where $\tilde{D}(\ )/Dt = \partial(\ )/\partial t + \tilde{U}_k(\ )/\partial x_k$, and $\tilde{\sigma}_c$ is the condensation rate; η_v and η_l are molecular diffusivities for Q_v and Q_l, respectively. The temperature will increase, due to latent heat

* A list of publications (up to May 1973) related to the BOMEX project is in BOMAP bulletin No. 12.

† Henceforth the phrase 'mixing ratio of' is omitted unless necessary to avoid confusion.

release by condensation, such that

$$\tilde{D}\tilde{\Theta}/Dt = \alpha\,\partial^2\tilde{\Theta}/\partial x_k^2 + (\Theta/T)(L_v/c_p)\tilde{\sigma}_c. \quad . \quad . \quad (3)$$

The potential temperature, $\tilde{\Theta}$, is related to the absolute temperature, $\tilde{T}$, according to

$$\tilde{\Theta} \equiv (P_0/P)^{\kappa}\tilde{T} = (\Theta/T)\tilde{T}. \quad . \quad . \quad . \quad (4)$$

In the above, P is the (ensemble mean) pressure; P_0 a reference pressure; κ the ratio of the gas constant for dry air, R_d, to the specific heat of air at constant pressure, c_p; and L_v the latent heat of evaporation.

When Eqs. (1) to (3) are converted into a mean and second-moment equations for Q_l, $\overline{q_l^2}$ and $\overline{wq_l}$ (appropriate to either subgrid-scale models or ensemble mean models), difficulties are encountered in dealing with the condensation rate term. If to simplify matters one assumes no supersaturation, then $\tilde{\sigma}_c$ is still a complicated discontinuous function of $\tilde{Q}_v$, $\tilde{Q}_l$ and the saturation mixing ratio of water vapour, $\tilde{Q}_s$.

An alternative method has been suggested (Sommeria and Deardorff 1977; Mellor 1977), in which the amount of condensation is obtained statistically. Towards this approach, one deals with two conserved quantities. First, we have

$$\tilde{D}\tilde{Q}_w/Dt = \eta_w\partial^2\tilde{Q}_w/\partial x_k^2, \quad . \quad . \quad . \quad (5)$$

where $\tilde{Q}_w$ is the mixing ratio of total water, defined by

$$\tilde{Q}_w \equiv \tilde{Q}_v + \tilde{Q}_l, \quad . \quad . \quad . \quad . \quad (6)$$

and η_w is the molecular diffusivity for $\tilde{Q}_w$. A second conservation equation is

$$\tilde{D}\tilde{\Theta}_l/Dt = \alpha_l\partial^2\tilde{\Theta}_l/\partial x_k^2, \quad . \quad . \quad . \quad (7)$$

where $\tilde{\Theta}_l$ is the liquid water potential temperature defined by

$$\tilde{\Theta}_l \equiv \tilde{\Theta} - (\Theta/T)(L_v/c_p)\tilde{Q}_l, \quad . \quad . \quad . \quad (8)$$

and α_l is the molecular diffusivity for $\tilde{\Theta}_l$. According to Betts (1973) '$\tilde{\Theta}_l$ represents the potential temperature attained by evaporating all the liquid water in an air parcel through reversible wet adiabatic descent'.

In order to recover the absolute temperature and properties of the condensed water field that are necessary for computing radiation cooling effects and buoyancy effects we shall assume a Gaussian probability distribution for $\tilde{\Theta}_l$ and $\tilde{Q}_w$; this will be discussed further in section 2(*c*). First we will derive equations for the mean variables and various turbulence moments.

(*b*) *Model equations*

The equations of motion with the Boussinesq approximation may be written as

$$\rho\{\tilde{D}\tilde{U}_j/Dt + \varepsilon_{jkl}f_k\tilde{U}_l\} = -\partial\tilde{P}/\partial x_j + \rho\{1-\beta(\tilde{\Theta}_v-\Theta_v)\}g_j + \mu\,\partial^2\tilde{U}_j/\partial x_k^2, \quad (9)$$

where $\tilde{\Theta}_v$ is a virtual potential temperature defined as $\tilde{\Theta}_v = \tilde{\Theta}(1+0{\cdot}61\,\tilde{Q}_w - 1{\cdot}61\,\tilde{Q}_l)$; $\beta g_j(\tilde{\Theta}_v - \Theta_v)$ is the buoyancy due to turbulent temperature fluctuations and $\beta \equiv 1/\Theta_v$ is the thermal expansion coefficient; $g_j = (0,0,-g)$ is the acceleration of gravity; $f_k = (0,f_y,f)$ is the Coriolis parameter; and μ is the molecular viscosity. Readers who wish to see greater details of the derivations of equations presented here may refer to Yamada (1978).

Decomposing the instantaneous values into ensemble means and fluctuations, the mean equations of motion may be obtained from Eqs. (9), (7) and (5) as

$$DU_j/Dt+\partial(\overline{u_k u_j})/\partial x_k+\varepsilon_{jkl}f_k U_l = -(1/\rho)(\partial P/\partial x_j)+g_j+\nu\,\partial^2 U_j/\partial x_k^2, \tag{10}$$

$$D\Theta_l/Dt+\partial(\overline{u_k\theta_l})/\partial x_k = \alpha_l\partial^2\Theta_l/\partial x_k^2, \tag{11}$$

and

$$DQ_w/Dt+\partial(\overline{u_k q_w})/\partial x_k = \eta_w\partial^2 Q_w/\partial x_k^2, \tag{12}$$

where ν is the kinematic viscosity and overbars represent ensemble averages. Equations (10) to (12) are not closed since terms such as $\overline{u_k u_j}$, $\overline{u_k\theta_l}$ and $\overline{u_k q_w}$ are not known. Since the derivation of the second-moment equations has been already presented by Mellor (1973), only a brief review on the closure assumptions is necessary here. In order to close the second-moment equations we use Rotta's hypothesis for the correlation between pressure and velocity gradient, Kolmogorov's isotropy hypothesis for the dissipation, and the assumption of down-gradient diffusion for triple moments. Subsequently Mellor and Yamada (1974) proposed a heirarchy of turbulence closure models from which the level 3 model was chosen to simulate the Wangara experiment (Yamada and Mellor 1975). A more recent study by Yamada (1977), however, indicates that a simpler model, which solves prognostically only the turbulence energy equation, reproduced quite well the Wangara simulation obtained by the level 3 model. This model is tentatively referred to as the level 2·5 model, since its complexity is between that of the level 2 and the level 3 models of Mellor and Yamada, and may be formally obtained from the level 3 model by omitting the advection, diffusion and tendency terms in all the second-moment equations for the scalar variables. The level 2·5 model is chosen for the present study.

The turbulence energy equation is

$$Dq^2/Dt-\partial/\partial x_k(q_l\tilde{S}_q\partial q^2/\partial x_k) = -2\,\overline{u_k u_i}\,\partial U_i/\partial x_k-2\beta g_k\overline{u_k\theta_v}-2q^2/\Lambda_1, \tag{13}$$

where $q^2=\overline{u_i u_i}$, $\tilde{S}_q$ is a function of stability and Λ_1 is a length scale, which will be described in subsection (*e*). The second term on the left is the modelled diffusion term for triple moments, and the last term is the modelled dissipation term due to Kolmogorov. The remaining terms are obtained from the Reynolds stress equations without further assumptions. Then the various remaining turbulence second moments (with the boundary layer approximation applied) may be obtained from the following set of algebraic equations which are similar, but not identical, to those given in Yamada and Mellor (1975).*

$$\begin{bmatrix}\overline{u^2}\\ \overline{v^2}\\ \overline{w^2}\end{bmatrix}-\tfrac{1}{3}q^2\begin{bmatrix}1\\1\\1\end{bmatrix}=(l_1/q)\begin{bmatrix}4P_{xx}-2P_{yy}-2\beta g\,\overline{w\theta_v}\\ -2P_{xx}+4P_{yy}-2\beta g\,\overline{w\theta_v}\\ -2P_{xx}-2P_{yy}+4\beta g\,\overline{w\theta_v}\end{bmatrix}, \tag{14a,b,c}$$

$$-\begin{bmatrix}\overline{uv}\\ \overline{uw}\\ \overline{vw}\end{bmatrix}=3(l_1/q)\begin{bmatrix}-P_{yx}-P_{xy}\\ (\overline{w^2}-C_1q^2)\partial U/\partial z-\beta g\,\overline{u\theta_v}\\ (\overline{w^2}-C_1q^2)\partial V/\partial z-\beta g\,\overline{v\theta_v}\end{bmatrix}, \tag{15a,b,c}$$

$$-\begin{bmatrix}\overline{u\theta_l}\\ \overline{v\theta_l}\\ \overline{w\theta_l}\end{bmatrix}=3(l_2/q)\begin{bmatrix}\overline{uw}\,\partial\Theta_l/\partial z+\overline{w\theta_l}\partial U/\partial z\\ \overline{vw}\,\partial\Theta_l/\partial z+\overline{w\theta_l}\partial V/\partial z\\ \overline{w^2}\,\partial\Theta_l/\partial z-\beta g\,\overline{\theta_v\theta_l}\end{bmatrix}, \tag{16a,b,c}$$

* In Mellor and Yamada (1974), a mistake was made. The last term in Eq. (21) of that paper, and subsequently all terms labelled D_1q^3 or D_f should be purged since they are of order a^2. The same correction should be applied in Yamada and Mellor. The numerical effects are small.

$$-\begin{bmatrix}\overline{uq}_w\\ \overline{vq}_w\\ \overline{wq}_w\end{bmatrix} = 3(l_2/q)\begin{bmatrix}\overline{uw}\,\partial Q_w/\partial z+\overline{wq}_w\partial U/\partial z\\ \overline{vw}\,\partial Q_w/\partial z+\overline{wq}_w\partial V/\partial z\\ \overline{w^2}\partial Q_w/\partial z-\beta g\,\overline{\theta_v q}_w\end{bmatrix}, \quad . \quad (17a,b,c)$$

$$-\overline{\theta_l q}_w = (\Lambda_2/2q)(\overline{w\theta_l}\partial Q_w/\partial z+\overline{wq}_w\partial\Theta_l/\partial z), \quad . \quad (18)$$

$$\overline{\theta_l^2} = (\Lambda_2/q)(-\overline{w\theta_l})\partial\Theta_l/\partial z, \quad . \quad . \quad (19)$$

and

$$\overline{q_w^2} = (\Lambda_2/q)(-\overline{wq}_w)\partial Q_w/\partial z. \quad . \quad . \quad (20)$$

In this analysis

$$P_{ij} \equiv -\overline{wu_i}\partial U_j/\partial z. \quad . \quad . \quad . \quad (21)$$

In the above expressions l_1, l_2 and Λ_2 are length scales which will be discussed in subsection (*e*), and C_1 is an empirical constant (Mellor and Yamada 1977). The terms on the left of Eqs. (14)–(17) are results of modelling the pressure–velocity gradient correlation terms according to Rotta's hypothesis. Similarly the first terms in Eqs. (18)–(20) employ Kolmogorov's hypothesis. Unlike the previous cases (Mellor and Yamada 1974; Yamada and Mellor 1975), the set of equations (10) to (20) is not yet closed due to the buoyancy terms, which involve the fluctuation of virtual potential temperature. Therefore, additional expressions to relate the terms $\overline{u_j\theta_v}$, $\overline{\theta_v\theta_l}$ and $\overline{\theta_v q_w}$ to known terms, resulting in Eqs. (41), (43b) and (45), are required; this is the subject of the following two sections.

(*c*) *Cloud model closure*

The object of the analysis in this section is to obtain expressions for the mean liquid water and various turbulence second-moments involving q_l, such as $\overline{u_j q_l}$, $\overline{q_l\theta_l}$, $\overline{q_l q_w}$, and $\overline{q_l^2}$. These terms are necessary to relate the term $\overline{u_j\theta_v}$ to the terms $\overline{u_j\theta_l}$ and $\overline{u_j q_w}$. Following Sommeria and Deardorff (1977), the probability density function, G, for the conserved variables $\tilde{\Theta}_l$ and $\tilde{Q}_w$ is assumed to be Gaussian such that

$$G = \{2\pi\sigma_{\theta l}\sigma_{qw}(1-r^2)^{\frac{1}{2}}\}^{-1}\exp[-(1-r^2)^{-1}\{\theta_l^2/2\sigma_{\theta l}^2 - r\theta_l q_w/\sigma_{\theta l}\sigma_{qw}+q_w^2/2\sigma_{qw}^2\}], \quad (22)$$

where $\sigma_{\theta l}^2 = \overline{\theta_l^2}$, $\sigma_{qw}^2 \equiv \overline{q_w^2}$ and $r \equiv \overline{\theta q_w}/\sigma_{\theta l}\sigma_{qw}$. As pointed out by Sommeria and Deardorff, it appears reasonable to assume joint-normal probability distributions for the quasi-conservative variables Θ_l and Q_w in the absence of precipitation or deep clouds. However, future research may dictate that the Gaussian assumption may be improved; for example, it may be necessary to add skewness to the distribution. Then the local condensation is assumed to be given by

$$\tilde{Q}_l = (\tilde{Q}_w-\tilde{Q}_s)\,H(\tilde{Q}_w-\tilde{Q}_s), \quad . \quad . \quad . \quad (23)$$

where $H(x)$ is a Heaviside function. Then, for example, the fraction of the volume occupied by clouds (henceforth, cloud volume), R, is

$$R = \int_{-\infty}^{\infty}\int_{-\infty}^{\infty} H(\tilde{Q}_w-\tilde{Q}_s)G\,d\tilde{Q}_w d\tilde{\Theta}_l, \quad . \quad . \quad (24)$$

which may be integrated analytically. However, first it is convenient to define

$$a \equiv (1+Q_{sl,T}(L/c_p))^{-1}, \quad . \quad . \quad . \quad (25a)$$

$$b \equiv a(T/\Theta)\,Q_{sl,T}, \quad . \quad . \quad . \quad (25b)$$

$$\Delta Q \equiv Q_w-Q_{sl}, \quad . \quad . \quad . \quad (25c)$$

$$Q_{sl,T} \equiv (\partial \tilde{Q}_s/\partial \tilde{T})_{\tilde{T}=T_l} = 0{\cdot}622(L_v/R_d)(Q_{sl}/T_l^2). \quad . \quad (26)$$

$$Q_{sl} = 0{\cdot}622 e_s(T_l)/(P - e_s(T_l)), \quad . \quad . \quad . \quad (27)$$

$$e_s(T_l) = e_0 \exp\{(L_v/R_w)(1/273 - 1/T_l)\}, \quad . \quad . \quad (28)$$

and

$$T_l \equiv (P/P_0)^{\kappa}\Theta_l, \quad . \quad . \quad . \quad (29)$$

where Q_{sl} is the mean saturation mixing ratio of water vapour at liquid water temperature T_l defined by Eq. (29), $e_s(T_l)$ is the saturation vapour pressure at T_l, and e_0 is the saturation water vapour at $T_l = 273$ K. Then Mellor (1977)* obtained the following expressions. For the cloud volume R, integration of Eq. (24) yields

$$R = \tfrac{1}{2}\{1 + \mathrm{erf}(Q_1/\sqrt{2})\}, \quad . \quad . \quad . \quad (30)$$

where $\mathrm{erf}(x) = (2/\sqrt{\pi})\int_0^x \exp(-y^2)\,dy$. Other integrations result in

$$Q_l/2\sigma_s = RQ_1 + (2\pi)^{-\frac{1}{2}}\exp(-Q_1^2/2), \quad . \quad . \quad (31)$$

where

$$Q_1 \equiv a\Delta Q/(2\sigma_s), \quad . \quad . \quad . \quad (32)$$

and

$$\sigma_s^2 = \tfrac{1}{4}(a^2\overline{q_w^2} - 2ab\,\overline{q_w\theta_l} + b^2\overline{\theta_l^2}). \quad . \quad . \quad (33)\dagger$$

Furthermore,

$$\overline{q_l\theta_l}/(a\,\overline{q_w\theta_l} - b\,\overline{\theta_l^2}) = R', \quad . \quad . \quad . \quad (34a)$$

$$\overline{q_l q_w}/(a\,\overline{q_w^2} - b\,\overline{q_w\theta_l}) = R', \quad . \quad . \quad . \quad (34b)$$

and

$$\overline{u_j q_l}/(a\,\overline{u_j q_w} - b\,\overline{u_j\theta_l}) = R', \quad . \quad . \quad . \quad (34c)$$

where we define

$$R' = R - (Q_l'/2\sigma_s)(2\pi)^{-\frac{1}{2}}\exp(-Q_1^2/2). \quad . \quad . \quad (35)$$

Finally, it can be shown that

$$\overline{q_l^2}/4\sigma_s^2 = R\{1 + (Q_1 - Q_l/2\sigma_s)^2\} + (Q_1 - 2Q_l/2\sigma_s)(2\pi)^{-\frac{1}{2}}\exp(-Q_1^2/2). \quad (36)$$

The relations (34a,b,c) are used in the next section to relate $\overline{u_j\theta_v}$ in Eqs. (14) to (17) to $\overline{u_j q_w}$ and $\overline{u_j\theta_l}$.

(d) *Fluxes involving* θ_v

Instantaneous virtual potential temperature is related to the liquid water potential temperature by

$$\tilde{\Theta}_v = (1 + 0{\cdot}61\tilde{Q}_w - 1{\cdot}61\tilde{Q}_l)\tilde{\Theta} = (1 + 0{\cdot}61\tilde{Q}_w - 1{\cdot}61\tilde{Q}_l)\{\tilde{\Theta}_l + (\Theta/T)(L_v/c_p)\tilde{Q}_l\}, \quad (37)$$

where Eq. (8) is used to obtain the second equality. Substituting $\tilde{\Theta}_v = \Theta_v + \theta_v$ etc. into Eq. (37), we obtain the mean virtual potential temperature as

$$\Theta_v \approx (1 + 0{\cdot}61Q_w - 1{\cdot}61Q_l)\{\Theta_l + (\Theta/T)(L_v/c_p)Q_l\}, \quad (38)$$

where higher-order terms, which include $\overline{q_w\theta_l}$, $\overline{q_w q_l}$, $\overline{q_l\theta_l}$ and $\overline{q_l^2}$, are omitted. Subtracting Eq. (38) from Eq. (37) we obtain the fluctuation of virtual potential temperature:

$$\beta\theta_v \approx \beta_T\theta_l + \beta_l q_l + \beta_w q_w, \quad . \quad . \quad . \quad (39)$$

* This reference includes a further reference to a corrigendum. The errors have been corrected here.
† An equivalent and convenient expression for σ_s^2 is given by Eq. (A. 12) in appendix A.

where again higher-order terms, which include $q_w\theta_l$, q_wq_l, $\overline{q_w\theta_l}$, $\overline{q_wq_l}$ etc., are omitted, and

$$\beta_T \equiv \beta(1+0{\cdot}61Q_w-1{\cdot}61Q_l), \quad . \quad . \quad . \quad . \quad (40a)$$

$$\beta_l \equiv \beta\{(1+0{\cdot}61Q_w-3{\cdot}22Q_l)(\Theta/T)(L_v/c_p)-1{\cdot}61\Theta_l\}, \quad . \quad (40b)$$

and

$$\beta_w \equiv 0{\cdot}61\beta\{\Theta_l+(\Theta/T)(L_v/c_p)Q_l\}. \quad . \quad . \quad . \quad (40c)$$

Multiplying both sides of Eq. (39) by u_j and taking an ensemble average we obtain

$$\beta\overline{u_j\theta_v} = \beta'_T\overline{u_j\theta_l}+\beta'_w\overline{u_jq_w}, \quad . \quad . \quad . \quad (41)$$

where Eq. (34) is used,

$$\beta'_T \equiv \beta_T-b\beta_lR' \quad . \quad . \quad . \quad (42a)$$

and

$$\beta'_w \equiv \beta_w+a\beta_lR'. \quad . \quad . \quad . \quad (42b)$$

Similarly multiplying both sides of Eq. (39) by θ_l and taking an average we obtain

$$\beta\overline{\theta_v\theta_l} = \beta_T\overline{\theta_l^2}+\beta_l\overline{q_l\theta_l}+\beta_w\overline{\theta_lq_w}. \quad . \quad . \quad (43a)$$

Next $\overline{\theta_lq_l}$ may be eliminated using Eq. (34a) to obtain

$$\beta\overline{\theta_v\theta_l} = -(\Lambda_2/2q)\{(\beta'_T\partial\Theta_l/\partial z+\mathscr{S})\overline{w\theta_l}+\beta'_w(\partial\Theta_l/\partial z)\overline{wq_w}\}, \quad . \quad (43b)$$

where Eqs. (18) to (20) are also used. In this relation

$$\mathscr{S} \equiv \beta'_T\partial\Theta_l/\partial z+\beta'_w\partial Q_w/\partial z. \quad . \quad . \quad . \quad (44)$$

In a similar fashion $\beta\overline{\theta_vq_w}$ may be expressed as

$$\beta\overline{\theta_vq_w} = -(\Lambda_2/2q)\{\beta'_T(\partial Q_w/\partial z)\overline{w\theta_l}+(\beta'_w\partial Q_w/\partial z+\mathscr{S})\overline{wq_w}\}, \quad . \quad (45)$$

where Eqs. (18) to (20) and (34b) are again used. Thus the set of equations (14) to (20), (41), (43b) and (45) is now closed. Vertical exchange coefficients are obtained from these equations as shown in appendix A to obtain various fluxes in Eqs. (50)–(55) which are summarized in section 3.

(e) *Length scale equation and empirical constants*

The equation to obtain a master length scale is the same as the one used by Mellor and Yamada (1977), which is the extension of a length scale equation for neutral stability discussed in Mellor and Herring (1973). The equation is given as

$$\frac{D}{Dt}(q^2l)-\frac{\partial}{\partial x_j}\{ql\tilde{S}_l\partial(q^2l)/\partial x_j\} = lE_1(-\overline{u_ju_i}\partial U_i/\partial x_j-\beta g_j\overline{u_j\theta_v})-(q^3/B_1)\{1+E_2(l/kz)^2\}, \quad (46)$$

where k is the von Kármán constant (0·4). The empirical constants E_1, E_2 and the stability function $\tilde{S}_l$ are discussed in Mellor and Yamada (1977) and are obtained as

$$(E_1, E_2, \tilde{S}_l) = (1{\cdot}8, 1{\cdot}33, 0{\cdot}2). \quad . \quad . \quad . \quad (47)$$

The rest of the length scales in the previous sections are assumed to be proportional to the master length scale, l, such that

$$(l_1, l_2, \Lambda_1, \Lambda_2) = (A_1, A_2, B_1, B_2)l. \quad . \quad . \quad (48)$$

The proportionality constants A_1, A_2, B_1 and B_2 were first determined from neutral laboratory experiments by Mellor (1973). Subsequent to examination of more data, as discussed in Mellor and Yamada (1977), the constants were altered slightly and are

$$(A_1, B_1, A_2, B_2, C_1, \tilde{S}_q) = (0{\cdot}92, 16{\cdot}6, 0{\cdot}74, 10{\cdot}1, 0{\cdot}08, 0{\cdot}2). \quad . \quad (49)$$

According to Yamada (1975), these numerical values agree well with those used by Lewellen and Teske (1973) but are much larger than those used by Deardorff (1973). However, it should be pointed out that the latter values are used for modelling subgrid-scale turbulence.

(*f*) *The grid system and the finite-difference approximation*

A log-plus-linear grid and a finite-difference scheme by Laasonen, described in detail in our previous paper (Yamada and Mellor 1975), are again used. A total of 80 points are distributed from the surface to the top of the grid (7·6 km). The grid interval increases log-linearly from 30 cm near the surface to 100 m in the upper layer.

3. One-dimensional equations, driving forces, and initial and boundary conditions

For the first attempt to incorporate condensation in the model we simplify to a one-dimensional calculation. However, it is possible to retain vertical advection terms for Θ_l and Q_w since the vertical velocity, W, can be estimated. Furthermore, we are able to estimate horizontal advections for Q_w. Therefore we have retained these particular advection terms.

$$\partial U/\partial t - fV = -(1/\rho)(\partial P/\partial x) + \partial(-\overline{uw})/\partial z \quad . \quad . \quad (50)$$

$$\partial V/\partial t + fU = -(1/\rho)(\partial P/\partial y) + \partial(-\overline{vw})/\partial z \quad . \quad . \quad (51)$$

$$\partial\Theta_l/\partial t + W\,\partial\Theta_l/\partial z = \partial(-w\theta_l)/\partial z + \sigma_r \quad . \quad . \quad (52)$$

$$\partial Q_w/\partial t + U\,\partial Q_w/\partial x + V\,\partial Q_w/\partial y + W\,\partial Q_w/\partial z = \partial(-\overline{wq}_w)/\partial z \quad . \quad (53)$$

$$\partial q^2/\partial t = \partial(q l \tilde{S}_q\,\partial q^2/\partial z)/\partial z + 2(P_{xx} + P_{yy} + \beta g\,\overline{w\theta_v}) - 2q^3/\Lambda_1 \quad . \quad (54)$$

$$\partial(q^2 l)/\partial t = \partial(q l \tilde{S}_l\,\partial q^2/\partial z)/\partial z - lE_1(P_{xx} + P_{yy} + \beta g\,\overline{w\theta_v}) - (q^3/B_1)\{1 + E_2(l/kz)^2\}, \quad (55)$$

where P_{ij} is defined by Eq. (21) and σ_r is the flux divergence of longwave radiation. All the fluxes in the above may now be related to mean variables as shown in Eqs. (A.1), (A.3), (A.4), (A.6) and (A.7) in appendix A, where K_M and K_H may be obtained by solving the simultaneous equations (A.10) and (A.11). A simplified radiation model (based on a fixed mixing ratio of water vapour profile and not yet taking advantage of predicted cloud volume) has been supplied to us by Dr S. Fels and Mr D. Schwarzkopf of the Geophysical Fluid Dynamics Laboratory. The vertical wind, W, is computed from wind profiles measured every 1½ h at four ships (Fig. 1) and the divergence equation, using a boundary condition $W = 0$ at $z = 0$. The result is shown in Fig. 2*. The horizontal pressure gradients $(1/\rho)(\partial P/\partial x)$ and $(1/\rho)(\partial P/\partial y)$ are time dependent and are obtained from the pressure profiles at four ship locations; they are computed by using the hydrostatic relation, the observed time-dependent temperature profiles and surface pressure. The results are shown in Figs. 3(a) and (b).

All the advection terms for Q_w are retained in order to see the importance of these terms in the sensitivity tests discussed in section 5. Horizontal advection terms for Q_w are approximated by the corresponding terms for the mixing ratio of water vapour which are computed from wind and water vapour measurements made at the four ships. The results are shown in Figs. 4(a) and (b) for $U\,\partial Q_v/\partial x$ and $V\,\partial Q_v/\partial y$, respectively.

* The authors are grateful to Dr E. Rasmusson and Mr T. Carpenter of the Center for Experiment Design and Data Analysis for a magnetic tape containing wind, temperature and water vapour data from which Figs. 2–6 are made.

Initial profiles of temperature, water vapour and wind are obtained by averaging the corresponding profiles observed at the four ships at 00 GMT* on 22 June 1969. The results are shown in Fig. 5. Approximate initial values for the turbulence moments, q^2, $\overline{\theta_l^2}$, etc., are generated using the relations obtained from the level 2 model approximation (Mellor and Yamada 1974; Yamada 1975). Under the level 2 model approximation all the turbulence moments can be obtained when mean variables are known. With these initial values the integration is performed for 1·5 h to obtain improved initial values for the turbulence moments. At this point the mean values are reinitialized to the 00 h values shown in Fig. 5 and the simulation is continued for four model days.

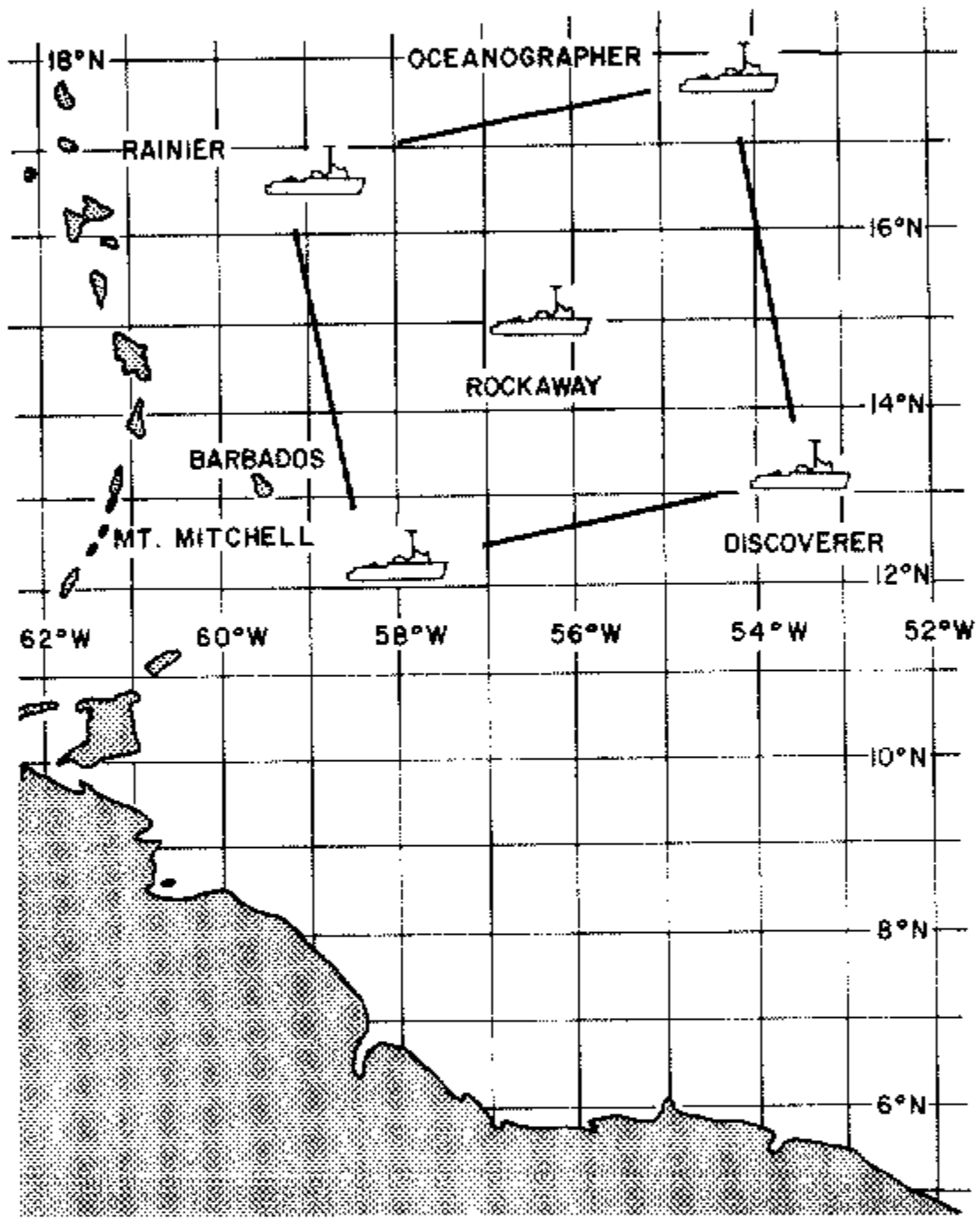

Figure 1. Location of ship array for BOMEX period III (22–29 June 1969).

Surface boundary conditions for wind and temperature are the same as those in Yamada and Mellor (1975), i.e.,

$$(U_1, V_1) = (U_2, V_2)\ln(z_1/z_0)/\ln(z_2/z_0), \quad . \quad . \quad (56)$$

and

$$\Theta_1 = \Theta_2\{\ln(z_1/z_{0t})/\ln(z_2/z_{0t})\} + \Theta_0\{1 - \ln(z_1/z_{0t})/\ln(z_2/z_{0t})\}, \quad . \quad (57)$$

where subscript 0 indicates the surface and subscripts 1 and 2 indicate the first and the second grids from the surface, respectively. The roughness length, z_0 is obtained (Charnock 1955) from

$$z_0 = 0{\cdot}016u_*^2/g, \quad . \quad . \quad . \quad (58)$$

* All times are Greenwich Mean Time, which is approximately four hours ahead of local standard time.

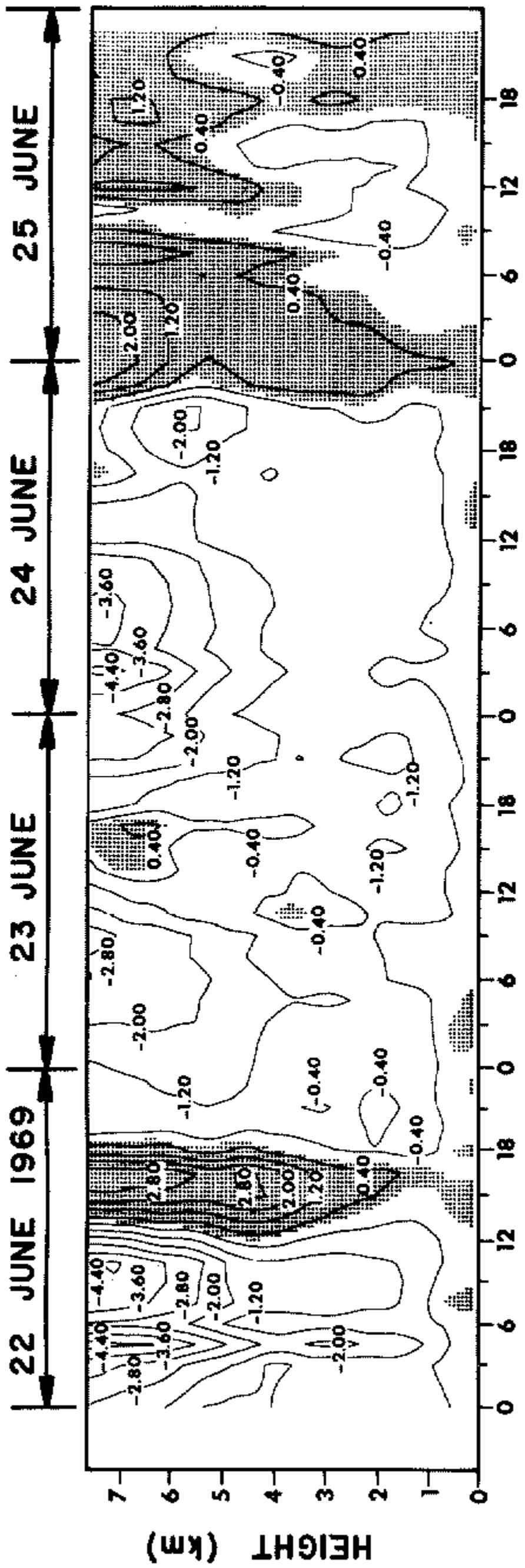

Figure 2. Vertical winds computed with the continuity equation from the horizontal wind profiles measured at four ships at the corners of the square array shown in Fig. 1. Units are cm s^{-1}.

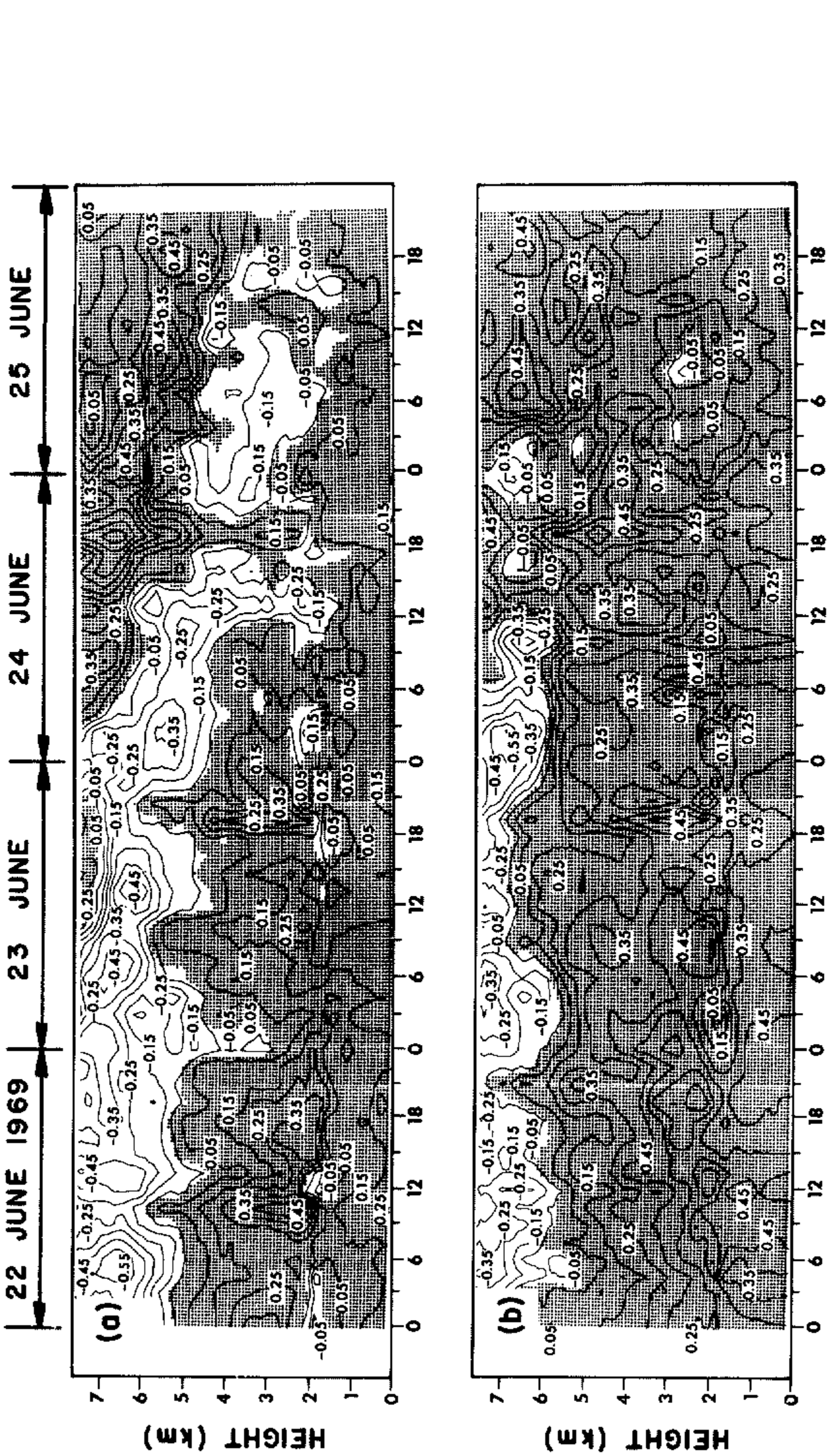

Figure 3. Horizontal pressure gradients: (a), $(1/\rho)(\partial P/\partial x)\times 10^3$; (b), $(1/\rho)(\partial P/\partial y)\times 10^3$; computed from the hydrostatic relation applied to temperature profiles measured at the four ships at the corners of the square array shown in Fig. 1. Units are $m\,s^{-2}$.

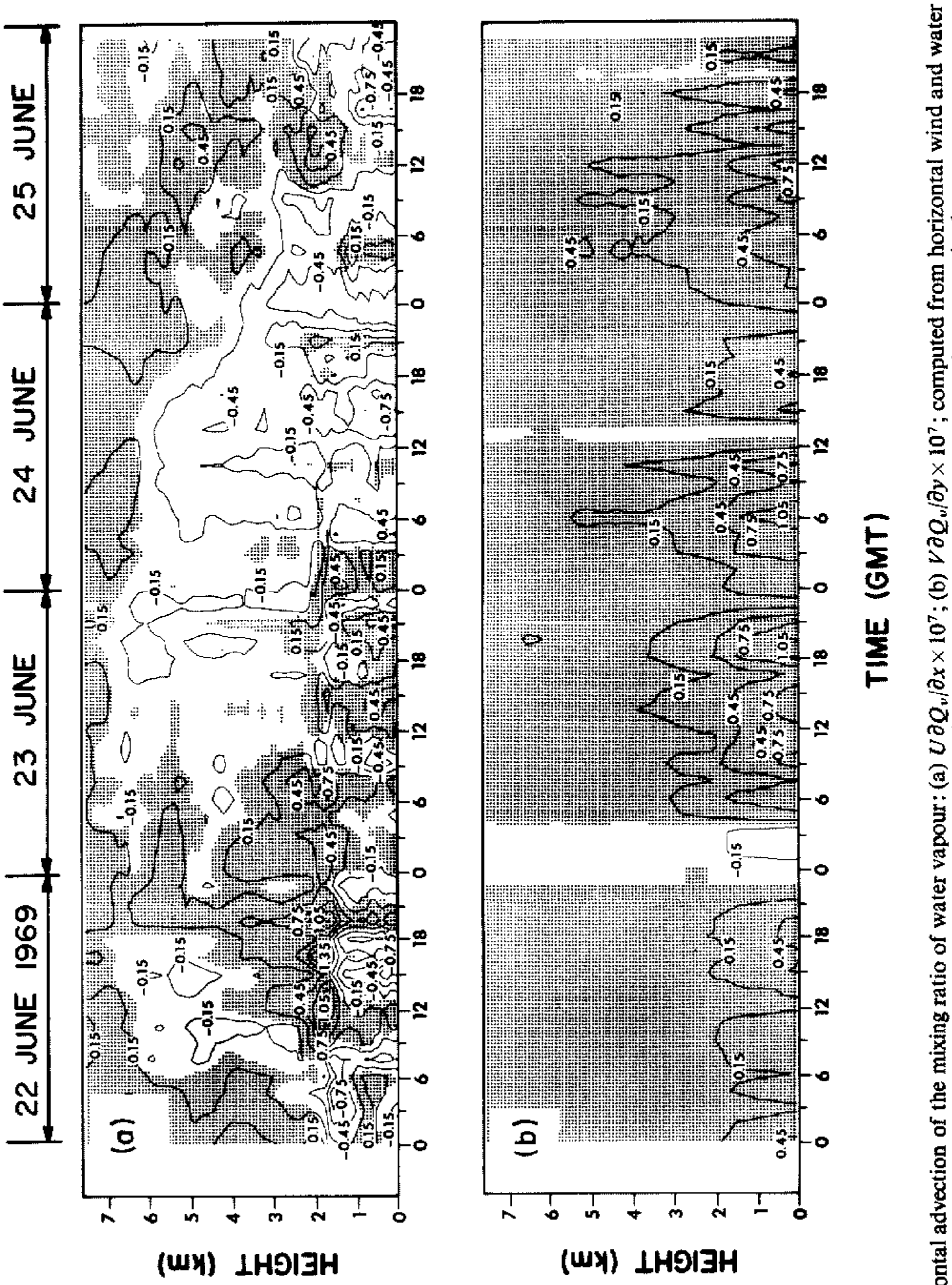

Figure 4. Horizontal advection of the mixing ratio of water vapour: (a) $U\partial Q_v/\partial x \times 10^7$; (b) $V\partial Q_v/\partial y \times 10^7$; computed from horizontal wind and water vapour profiles measured at four ships at the corners of the square array shown in Fig. 1. Units are $g\,g^{-1}s^{-1}$.

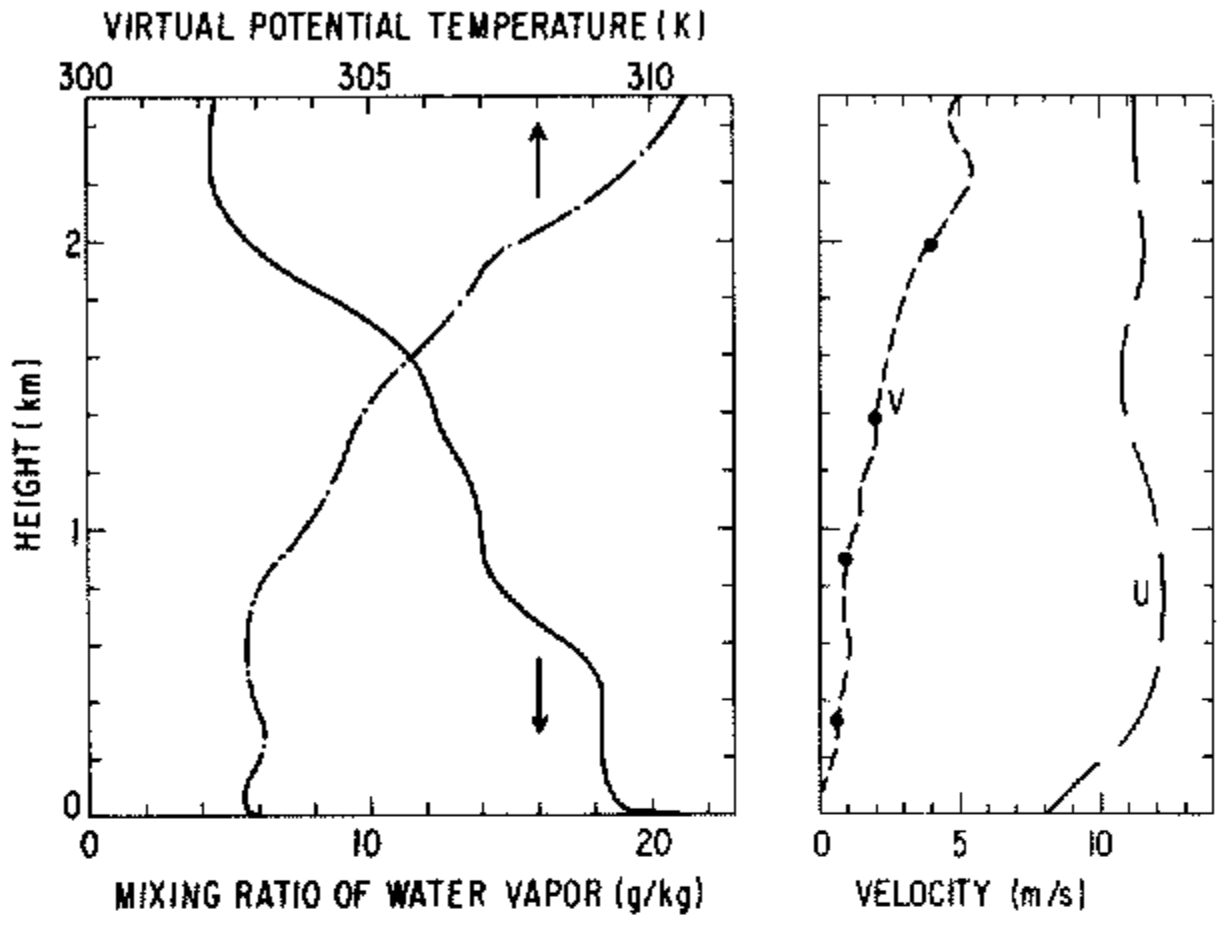

Figure 5. Mixing ratio of water vapour, virtual potential temperature, and horizontal wind at 00 h on 22 June, obtained by averaging the corresponding profiles measured at four ships at the corners of the square array shown in Fig. 1. These profiles are used as intitial values of the mixing ratio of total water, liquid water potential temperature and horizontal wind, respectively.

and z_{0t} is obtained (Sverdrup 1951; Sheppard 1958) from

$$z_{0t} = \alpha/ku_*, \quad . \quad . \quad . \quad . \quad (59)$$

where u_* is the friction velocity, and the constant 0·016 in Eq. (58) is obtained from Wu (1969). Surface temperature, Θ_0, is approximated by averaged air temperature ($z \approx 8$ m) measured at the four ships (Fig. 6). According to Paulson *et al.* (1972), air temperature at 11 m above the surface six weeks earlier than the present simulation period showed diurnal variations similar to that of surface temperature. Since surface temperature measurements were not available during period III, the air temperature as shown in Fig. 5 is used as a first approximation to the surface temperature.

A surface boundary condition similar to Eq. (57) is used for Q_w, i.e.,

$$Q_{w1} = Q_{w2}\{\ln(z_1/z_{0w})/\ln(z_2/z_{0w})\} + Q_{w0}\{1 - \ln(z_1/z_{0w})/\ln(z_2/z_{0w})\}, \quad (60)$$

where the roughness height z_{0w} is obtained (Sverdrup 1951; Sheppard 1958) from

$$z_{0w} = \eta_v/ku_*, \quad . \quad . \quad . \quad . \quad (61)$$

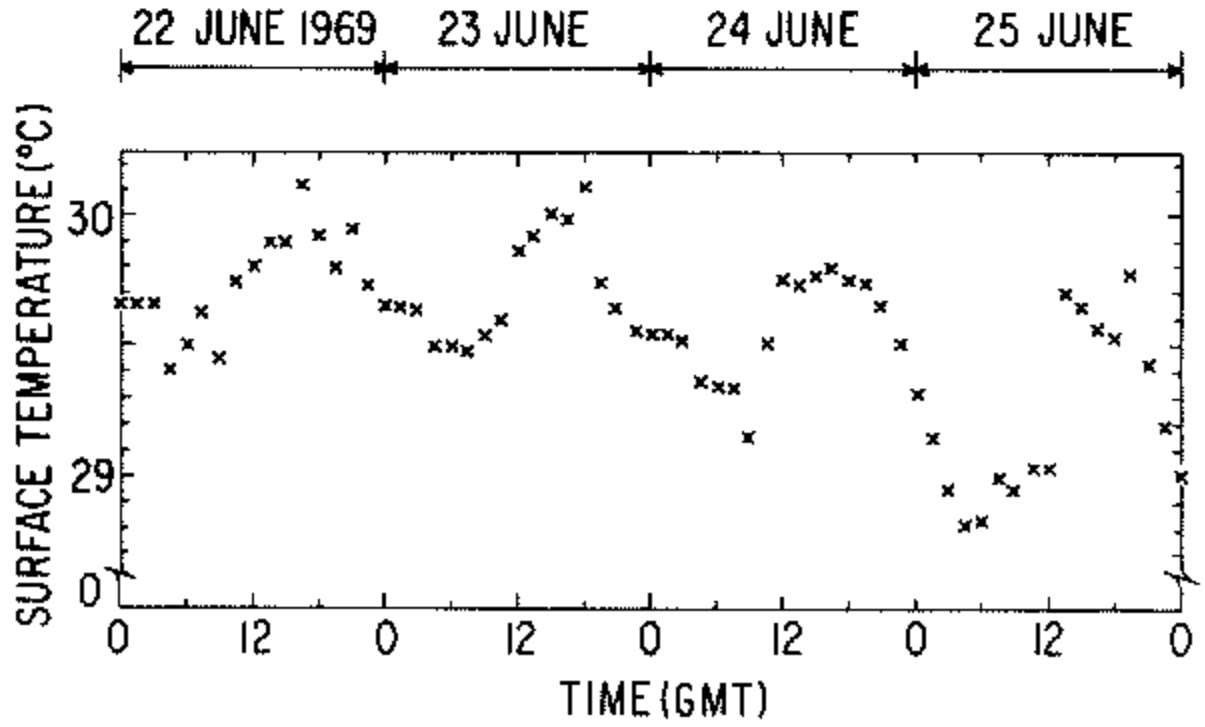

Figure 6. Observed surface ($z \approx 8$ m) air temperature variations, being the averages of the values measured at four ships at the corners of the square array shown in Fig. 1.

where η_v is the molecular diffusivity for water vapour. The surface value, Q_{w0}, is obtained by assuming that the surface is saturated so that

$$Q_{w0} = 0{\cdot}622\, e_s(\Theta_0)/(P_0 - e_s(\Theta_0)), \quad . \quad . \quad (62)$$

where the saturation water vapour pressure, $e_s(\Theta_0)$, is given by

$$e_s(\Theta_0) = 6{\cdot}11 \exp\{(L_v/R_v)(1/273 - 1/\Theta_0\}. \quad . \quad . \quad (63)$$

The surface boundary condition for Eq. (54) can be shown to be $q^2(0) = B_1^{\frac{2}{3}} u_*^2$. For the length scale equation, $l = kz$ is prescribed for the first two gridpoints above the surface.

At the upper boundary ($z = 7{\cdot}6$ km)

$$\partial U/\partial z = \partial V/\partial z = 0, \quad . \quad . \quad . \quad (64a)$$

$$\partial \Theta_l/\partial z = 0{\cdot}002 \text{ K m}^{-1}, \quad . \quad . \quad . \quad (64b)$$

and

$$\partial Q_w/\partial z = 0, \quad . \quad . \quad . \quad . \quad (64c)$$

where the temperature gradient in Eq. (64b) is obtained from the mean of observed temperature profiles. The upper boundary conditions $q^2 = 0$ and $q^2 l = 0$ are used for Eqs. (54) and (55), respectively.

Generally speaking, the upper boundary conditions are not as critical as the surface boundary conditions for the present simulation. The conditions for q^2 and $q^2 l$ are easily satisfied, since turbulence becomes very small in the inversion layer. Under these circumstances mean variables above the height where turbulence vanishes are effectively decoupled from the lower layer and do not contribute significantly to the dynamics of the boundary layer as addressed in the present study.

4. Results and discussion

Discussion is divided into two parts. In the first, simulated mean variables (horizontal wind speed, virtual temperature and water vapour) are compared with the BOMEX data. In the second, simulated cloud-related variables (mean liquid water, cloud volume and liquid water variance), turbulence energy, eddy viscosity coefficients, and a master length scale, are presented. The surface turbulent fluxes (heat, moisture and momentum) are compared with observations made six weeks earlier (Paulson *et al.* 1972), which are the only data readily available for comparison from BOMEX.

(a) *Mean horizontal wind, temperature and mixing ratio of water vapour*

Both simulated and observed mean wind, temperature and mixing ratio of water vapour in the boundary layer varied slowly during the simulation period. Therefore, only the results for the last day of simulation (25 June) are discussed here. Simulated horizontal wind speeds are compared with the observations in Fig. 7. The winds, particularly in the

simulations, are almost uniform with height, indicating strong mixing by turbulence. Indeed, the gradient Richardson number based on the simulated virtual potential temperature is found to be always negative from the surface to at least the cloud base. Simulated horizontal wind speeds within the first kilometre above the surface in earlier days (not shown here) also agree quite well with the data. However, uniform winds are not maintained

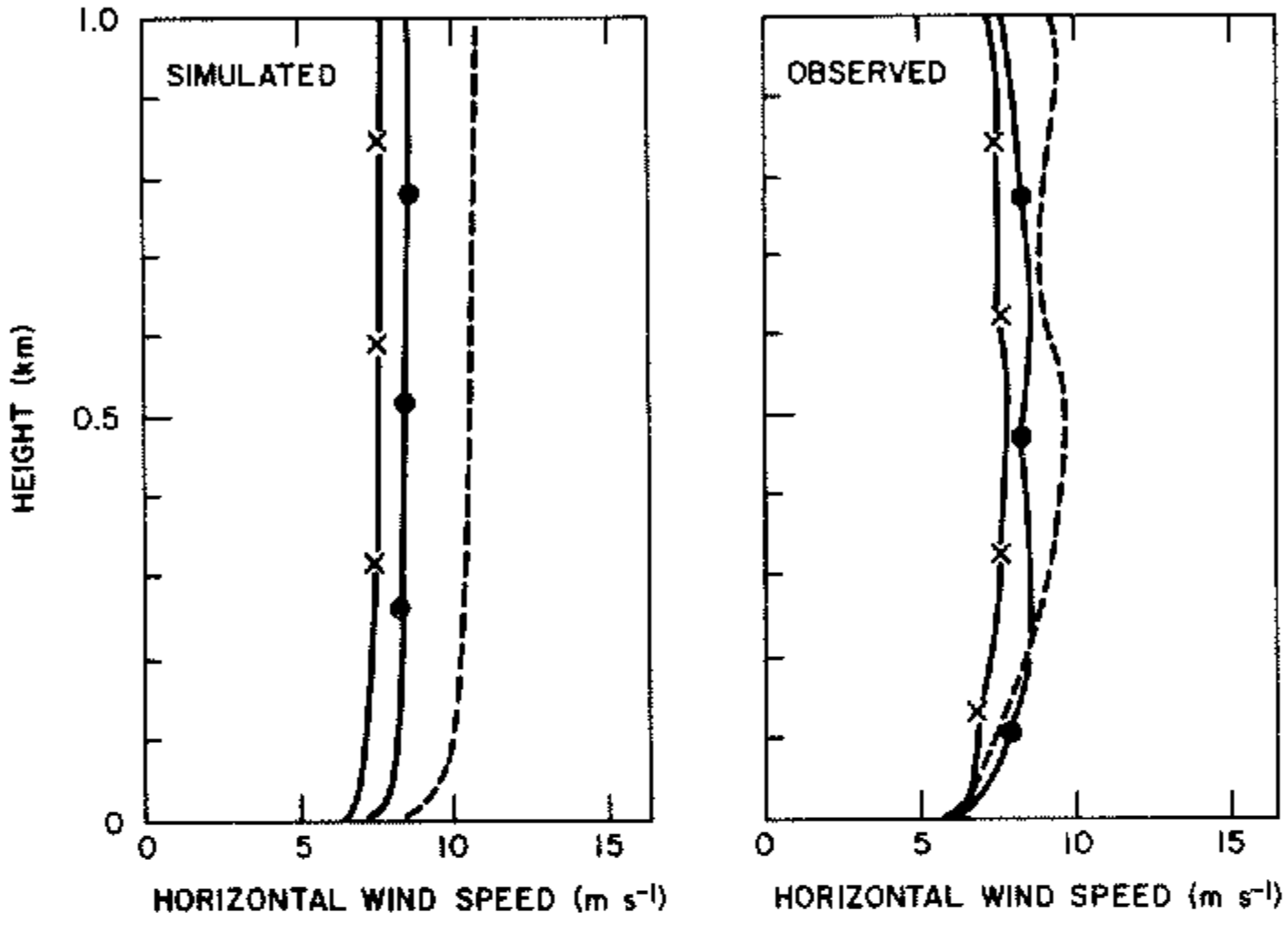

Figure 7. Simulated and observed horizontal wind speeds at 09 h (dashes), at 15 h (circles), and at 18 h (crosses) on 25 June.

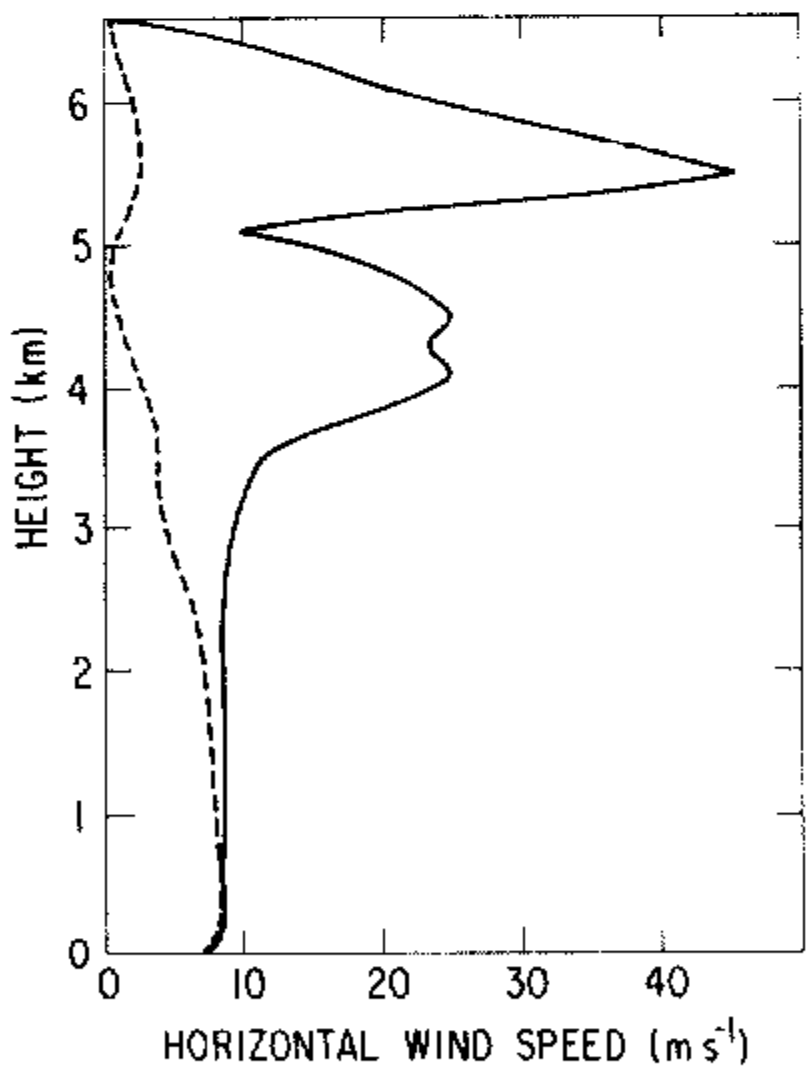

Figure 8. Simulated (continuous) and observed (dashed) horizontal wind speed at 15 h on 25 June.

in the upper layer (above 3 km for 25 June), where simulated horizontal wind profiles (Fig. 8) show large vertical shears. These latter profiles are dominated by horizontal pressure gradients (Fig. 3) obtained hydrostatically from vertical integration of the horizontal temperature gradients, which may be subject to considerable error. For example, a measurement error of 0·5 K/500 km in the horizontal temperature gradient results in an error of $1{\cdot}7 \times 10^{-4} \mathrm{m\,s^{-2}}$ in the horizontal pressure gradient at 5 km above the surface. Another

possible, but quantitatively less significant, cause for the large discrepancy between observed and simulated wind profiles is advection, which was not included in the present one-dimensional simulation.

Simulated virtual temperatures in the first 1600 m above the surface at 15 h (Fig. 9) are found to be slightly unstable, and about 2 K higher than observations, possibly because the surface temperature used as the boundary condition (ship measurements ~8 m above the surface) is too high. This is consistent with the fact that surface temperatures observed in the same area six weeks earlier (Paulson *et al.* 1972) were about 2 K lower than the surface boundary condition used in our simulation. This point is discussed further in section 5, where sensitivity of the surface temperature variation to the simulated mixing ratio of water vapour is examined. On the other hand, simulated temperatures in the layer

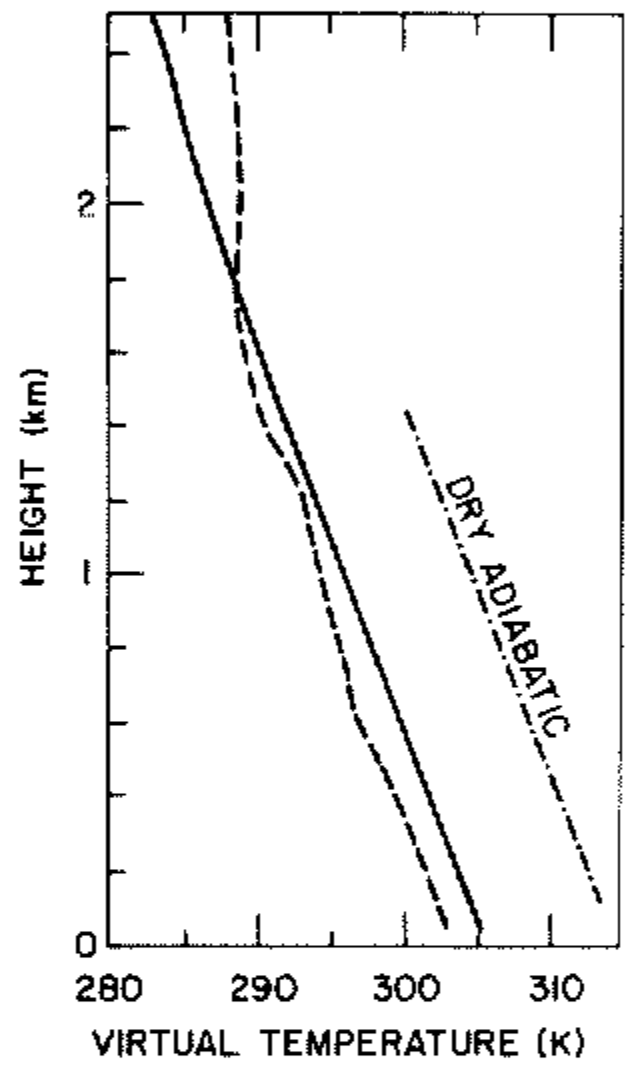

Figure 9. Simulated (continuous) and observed (dashed) virtual temperature at 15 h on 25 June.

above 1600 m are found to be about 2–3 K lower than observations. Causes for this discrepancy are unknown. However, since subsidence is the major source of warming in this model, the lower temperatures in the inversion layer may be due to underestimation of subsidence in the simulation, which is quite possible considering that the vertical wind used (Fig. 2) is the average over the 500 km × 500 km square.

Water vapour plays particularly important roles in the PBL over tropical oceans due to alteration of air density and release of latent heat by condensation. For example, potential temperature profiles over tropical oceans often indicate slight stability. However, the density stratification of the moist air is unstable because of the relatively large negative vertical gradient of water vapour. This unstable PBL is particularly important where water vapour is transported upwards by turbulence from the ocean to the cloud base. The latent heat released by condensation produces locally unstable layers, resulting in the generation of turbulence. Therefore, accurate simulation of water vapour is essential for better prediction of clouds and turbulence over tropical oceans. Figure 10 shows profiles of simulated and observed water vapour. The former agree quite well with observations in the first 600 m above the surface but simulations above 1 km are found to be approximately 1·5 g kg^{-1} more moist than observations. Simulated water vapour at 18 h was not distinguishable from that at 15 h. If subsidence greater than that shown in Fig. 2 had been used, the simulated mixing ratio of water vapour would have been much lower, since air in the upper layers is

relatively dry, and agreement with observations would have been much closer. This again suggests that accurate vertical wind variations are essential for better prediction of the mixing ratio of water vapour as well as for temperature. Surface temperature, from which the surface mixing ratio of water vapour is determined, and the horizontal advection of water vapour, are also important. Sensitivity of these variables to the simulated water vapour is discussed in section 5.

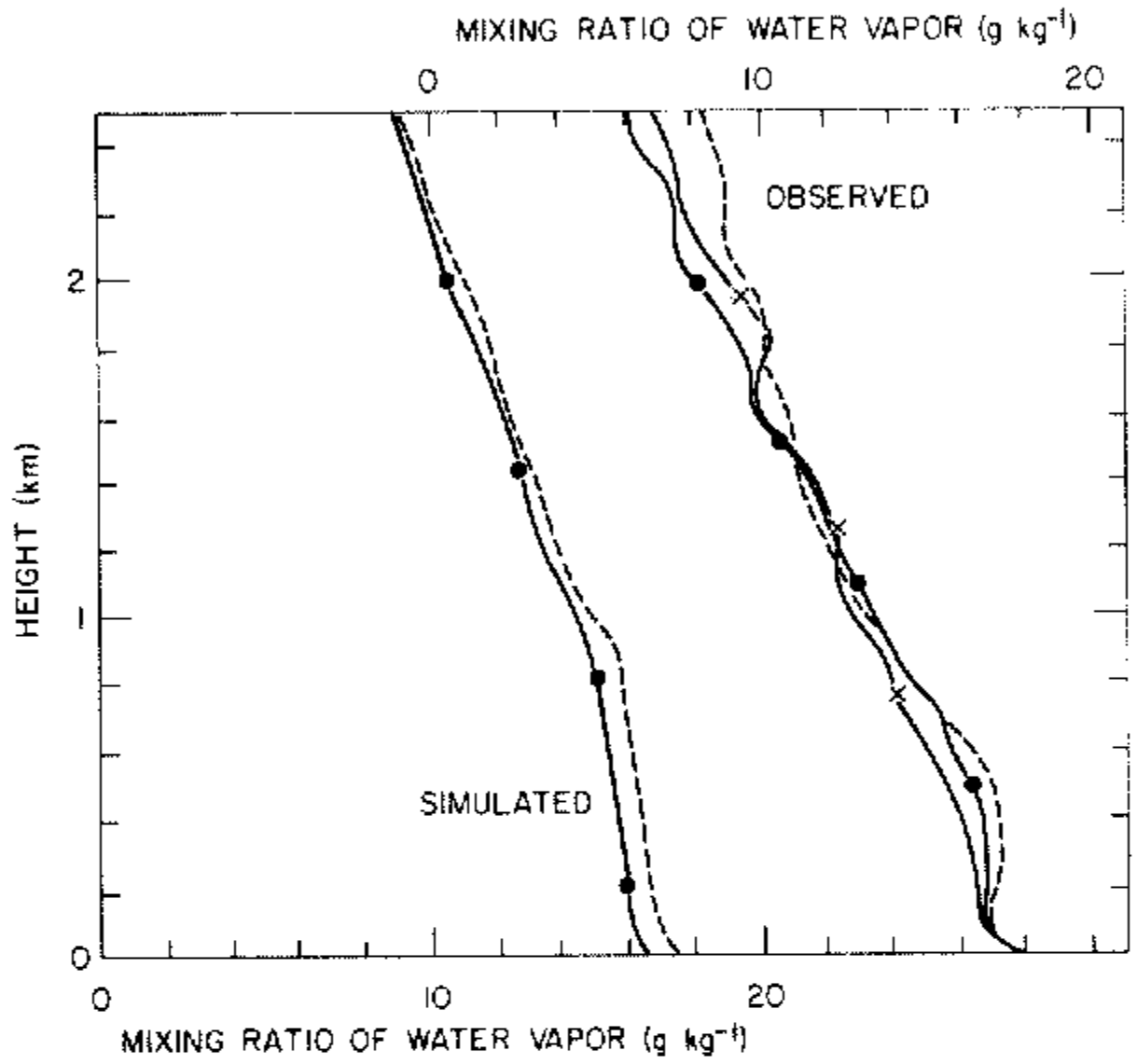

Figure 10. Simulated and observed water vapour at 09 h (dashes), 15 h (circles), and 18 h (crosses) on 25 June; note shift of coordinates between simulated and observed profiles. Simulated water vapour at 18 h was not distinguishable from that at 15 h.

As far as simulations of mean wind, temperature and water vapour are concerned, simpler models than the present one might have produced results similar to those presented here provided that effects of stability are properly included in the parametrization of turbulence. However, no simple parametrization of turbulence associated with cloud formation has yet been proposed. Thus, the present model has a great advantage over simpler models in this regard, as discussed in detail in the following section.

(*b*) *Clouds, turbulence, length scale and surface turbulent fluxes*

Unlike the mean variables discussed in the previous subsection, simulated cloud-related variables such as liquid water, cloud volume, and turbulence generated by the latent heat released by condensation, varied considerably with time. Such variations are particularly well demonstrated in the simulations for the last two days (24–25 June). Corresponding results for the first two days (22–23 June) showed the magnitude of these variables to be much smaller, and the vertical extent much less, than for 24–25 June.

All the simulated variables presented here, except turbulence energy and length scale, are obtained from the appropriate diagnostic equations discussed in section 2. Only qualitative discussion of the simulated results is possible since data for direct comparison are not available. Nevertheless the results presented here appear to be very useful to the understanding of atmospheric behaviour over tropical oceans.

Simulated mixing ratio of liquid water is computed from Eq. (31) and the results at 06 h and 15 h on 24 June are shown in Fig. 11(a). These hours correspond approximately to the times of surface temperature minimum and maximum, respectively (see Fig. 6). The amount of condensation predicted by the present model is a continuous function of the difference between the actual mixing ratio of water vapour and the saturation value.

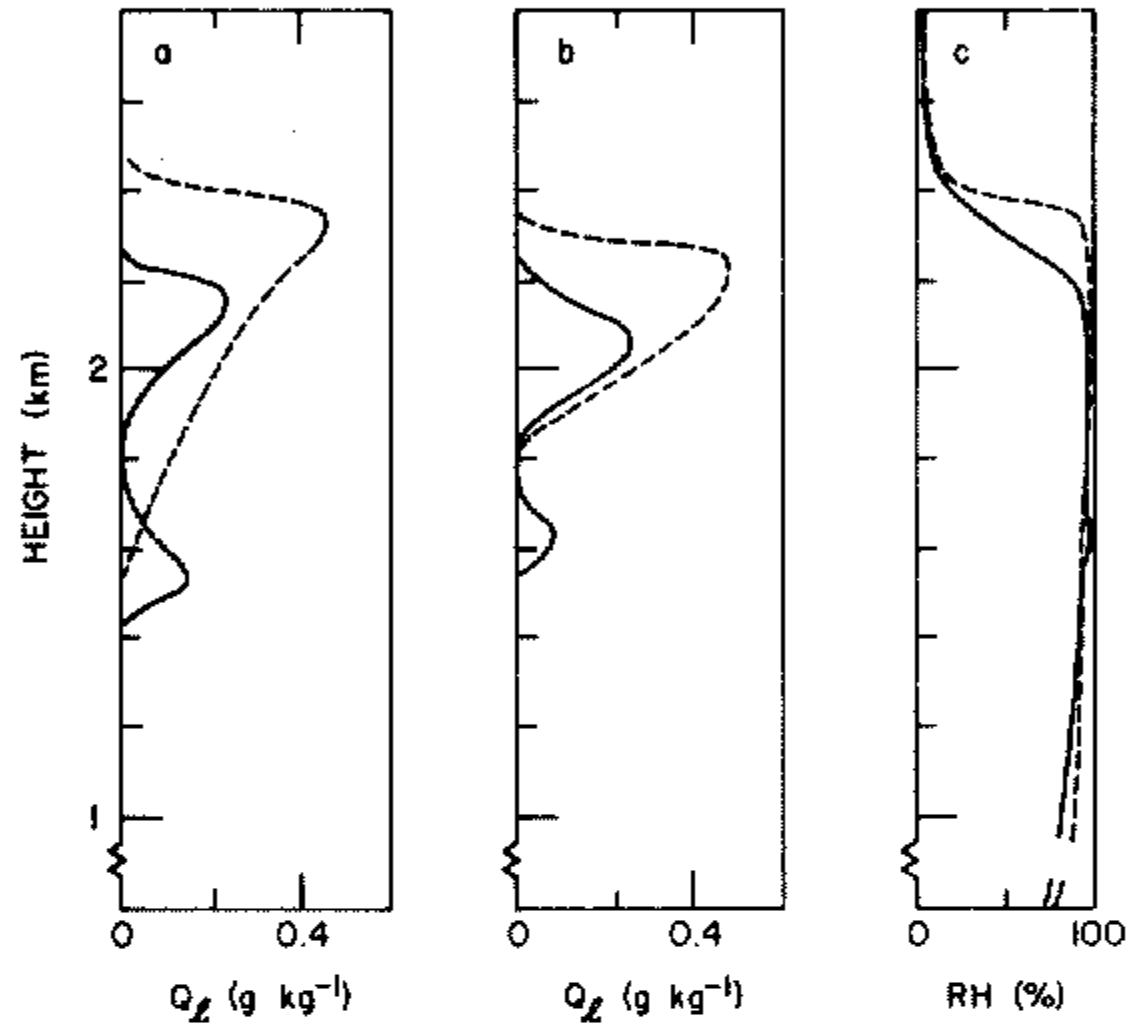

Figure 11. Simulated mixing ratio of liquid water at 06 h (continuous) and 15 h (dashes) on 24 June obtained (a) from the present model; (b) from an instantaneous condensation model in which a condensation criterion of 96% saturation is assumed. Simulated relative humidity profiles shown in (c) apply to either model.

If a conventional, instantaneous condensation scheme had been used, a diagnostic study indicates that close agreement with the present results might have been obtained if condensation had been assumed to occur at 96% saturation. The results are depicted in Fig. 11(b), and vertical profiles of relative humidity are given in Fig. 11(c). If the condensation criterion is changed by $\pm 1\%$, the mixing ratio of liquid water at 15 h is changed by approximately $\pm 10\%$. An even larger ($\pm 25\%$) variation for liquid water is found at 06 h. Thus, the amount of condensation for the conventional model is, as expected, very sensitive to the assumed condensation criterion: this appears to be a serious disadvantage compared with the present ensemble cloud model, since there seems to be no easy way to determine *a priori* the condensation criterion applicable to a general case.

Simulated cloud volume is computed from Eq. (30) and the results are given in Fig. 12(a). Observed cloud coverage in satellite pictures over the BOMEX area (BOMEX Atlas of Satellite Cloud Photographs, 1971) was variable, averaging about 30%. On the other hand, simulated cloud volume is less than 20% on the first day simulation but increases to as much as 80% on the fourth day. This increase appears to be caused by the overprediction of water vapour, as already discussed in conjunction with Fig. 10.

Root-mean-square values of the simulated variances of liquid water are computed from Eq. (36) and are shown in Fig. 12(b). The r.m.s. of the variance for liquid water (Fig. 12(b)) and the mean values of liquid water (Fig. 11(a)) become nearly equal, as seen from Eqs. (31) and (36), when Q_1 is close to zero (the present case).

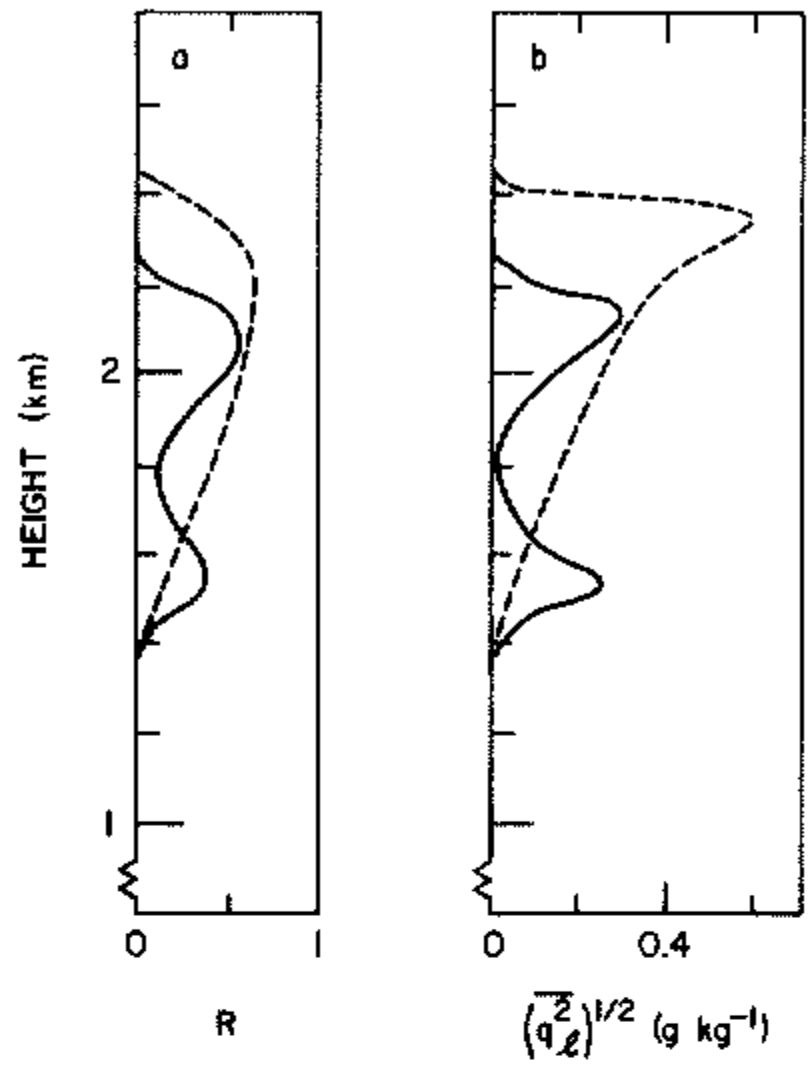

Figure 12. (a) Simulated cloud volume; (b) simulated r.m.s. of the variance for liquid water, at 06 h (continuous) and 15 h (dashed) on 24 June.

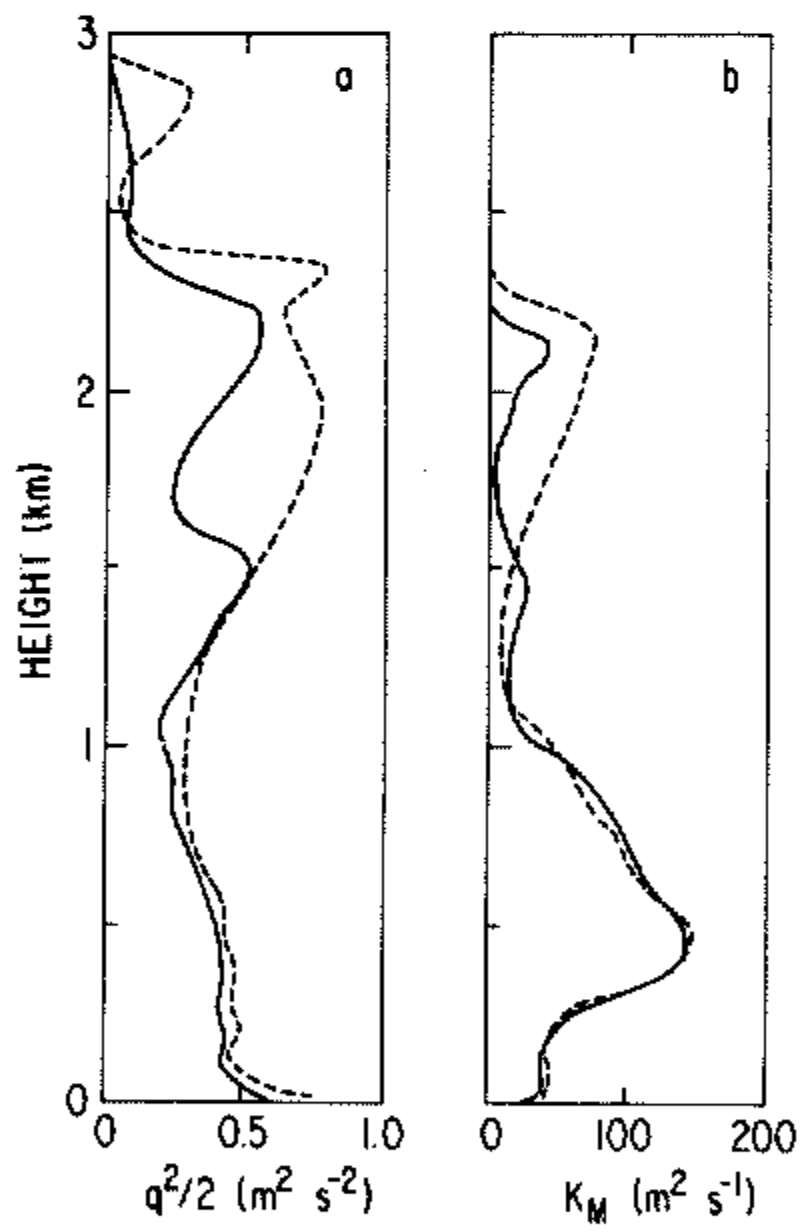

Figure 13. (a) Simulated turbulence energy, (b) simulated eddy viscosity coefficients, at 06 h (continuous) and 15 h (dashed) on 24 June.

The latent heat released by condensation increases the local temperature by approximately 0·5 K. This small increase of temperature is found to be sufficient to produce a locally unstable layer, which in turn generates turbulence. Figure 13(a) shows the simulated turbulence energy, $q^2/2$, computed prognostically from Eq. (54), for 24 June. The turbulence energy in the lowest kilometre shows a profile typical of an unstable PBL for clear days (Fig. 13(a)). However, the turbulence energy in the layer above 1 km is generated by buoyancy associated with condensation. The vertical profile of turbulence energy in this layer

correlates very well with that of liquid water (Fig. 11(a)). Eddy viscosity coefficients (Fig. 13(b)) are computed by solving Eqs. (A.10) and (A.11), and correlate very well with turbulence energy (Fig. 13(a)) and also with the liquid water (Fig. 11(a)) in the layer above 1 km.

Absorption and scattering of incoming solar radiation by clouds are important but are not in the scope of the present study. Atmospheric cooling due to longwave radiation is treated only in a simple manner, as discussed in section 3.

A master length scale, l, which was computed prognostically from Eq, (55) with the empirical constants given in Eq. (47), was found to increase sharply above the height where turbulence became small. The length scale was found to be as large as 600 m at 4 km above the surface. Such a large value of l was obtained when a finite value of $q^2 l$ determined from Eq. (55) was divided by a very small value of q^2. It is not clear whether l should decrease or increase at the heights where turbulence is almost absent. However, numerical procedures become much simpler if l is assumed to vanish near the upper boundary. To achieve this, an exponential increase of the empirical constant E_2 in Eq. (55) with height is assumed:

$$E_2 = 1{\cdot}33 \exp(z/500), \qquad (64)$$

where z is height (m). Simulated length scales on 24 June are shown in Fig. 14. The length scale above 3 km is probably meaningless since turbulence there is too small (see Fig. 13(a)). The length scale equation is still under study and Eq. (64) is a temporary expedient.

The simulated liquid water at 06 h on 25 June (Fig. 15(a)) shows a three-layered structure. This feature is also reflected in the profiles for cloud volume (Fig. 15(b)) and r.m.s. of

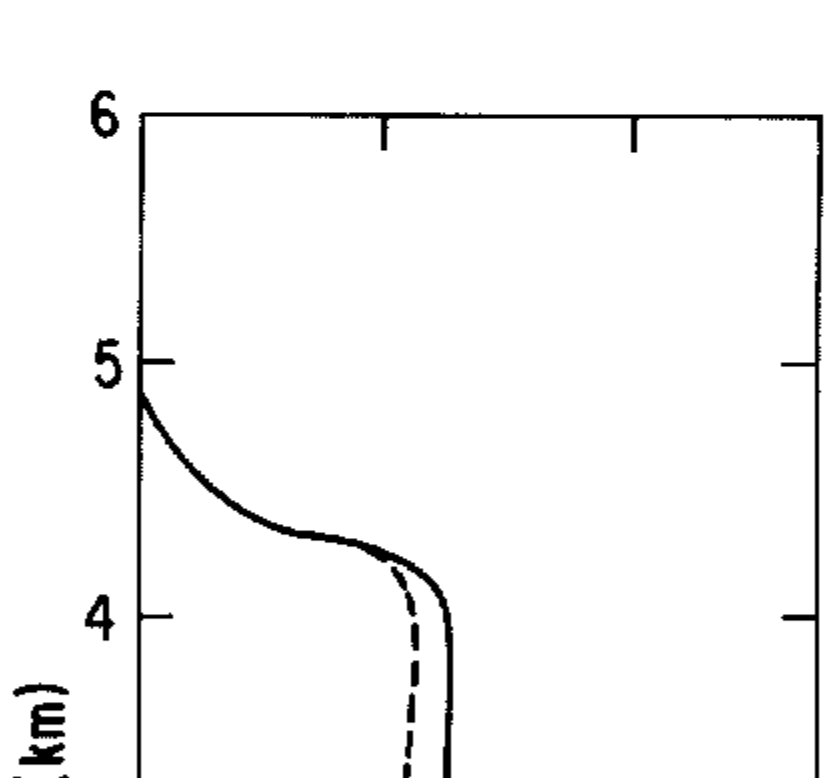

Figure 14. Simulated master length scale at 06 h (continuous) and 15 h (dashed) on 24 June.

the variance for liquid water (Fig. 15(c)). The layered cloud structures depicted in Figs. 11 and 15 are probably due to the one-dimensionality of the present model. Water vapour is continuously supplied from the ocean, transported upwards by turbulence and vertical wind and removed by winds (and/or precipitation, which is not considered here). As mentioned earlier, the horizontal advection terms in the equation for Q_w (Fig. 4) are input from data and are not necessarily consistent with the remaining terms, which are computed in the model. Inconsistency between computed and input terms might have disturbed cloud profiles, resulting in the layered structure shown in Figs. 11 and 15. Simulated turbulence energy and eddy viscosity coefficients are given in Figs. 16(a) and (b), respectively. Finally,

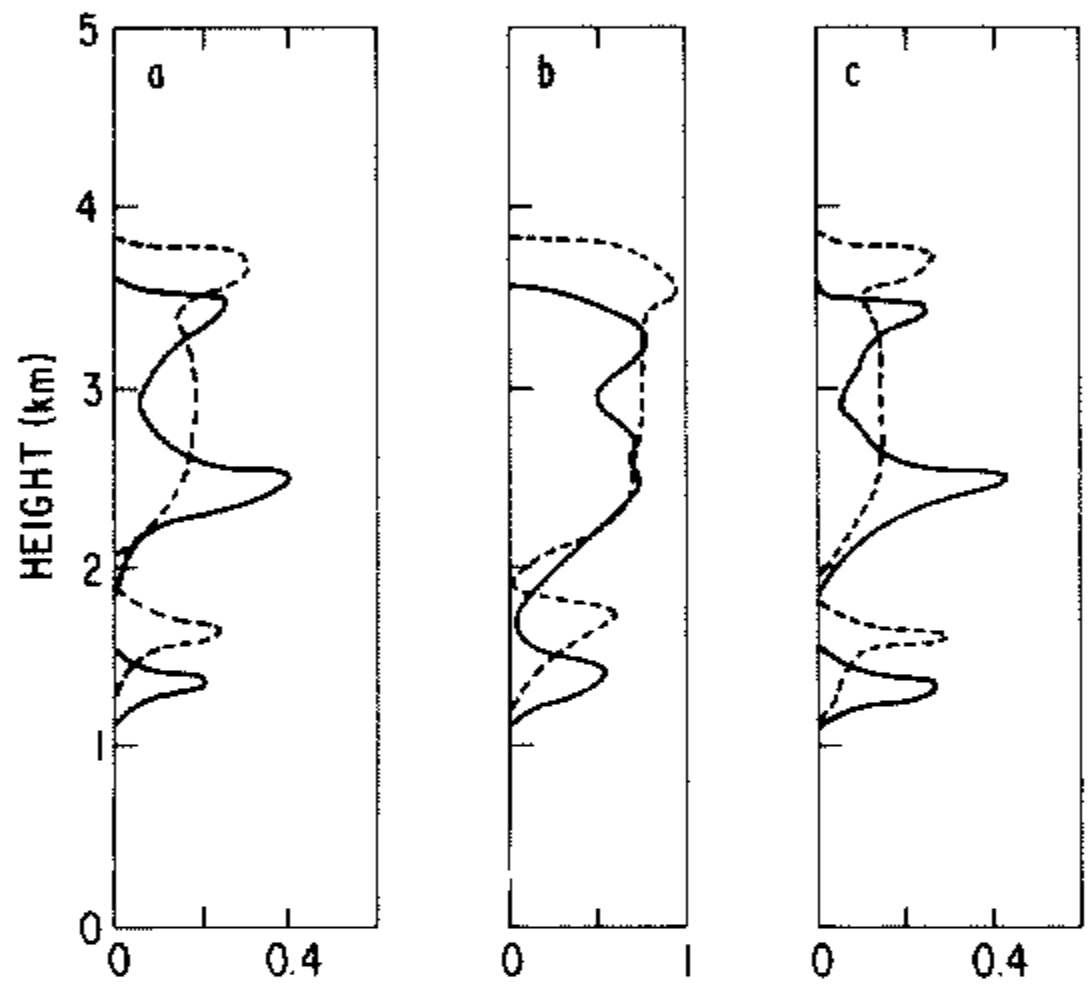

Figure 15. (a) Simulated liquid water, (b) simulated cloud volume, (c) simulated r.m.s. of the variance for liquid water, at 06 h (continuous) and 15 h (dashed) on 25 June.

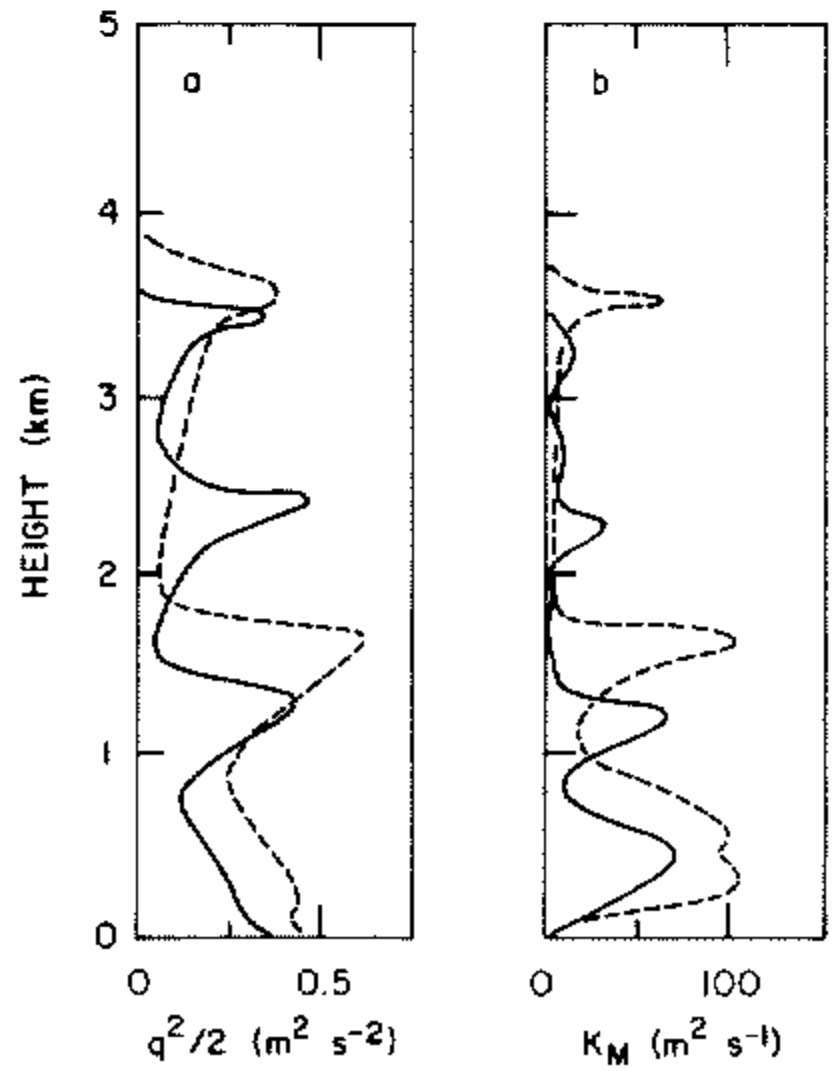

Figure 16. (a) Simulated turbulence energy, (b) simulated eddy viscosity coefficients, at 06 h (continuous) and 15 h (dashes) on 25 June.

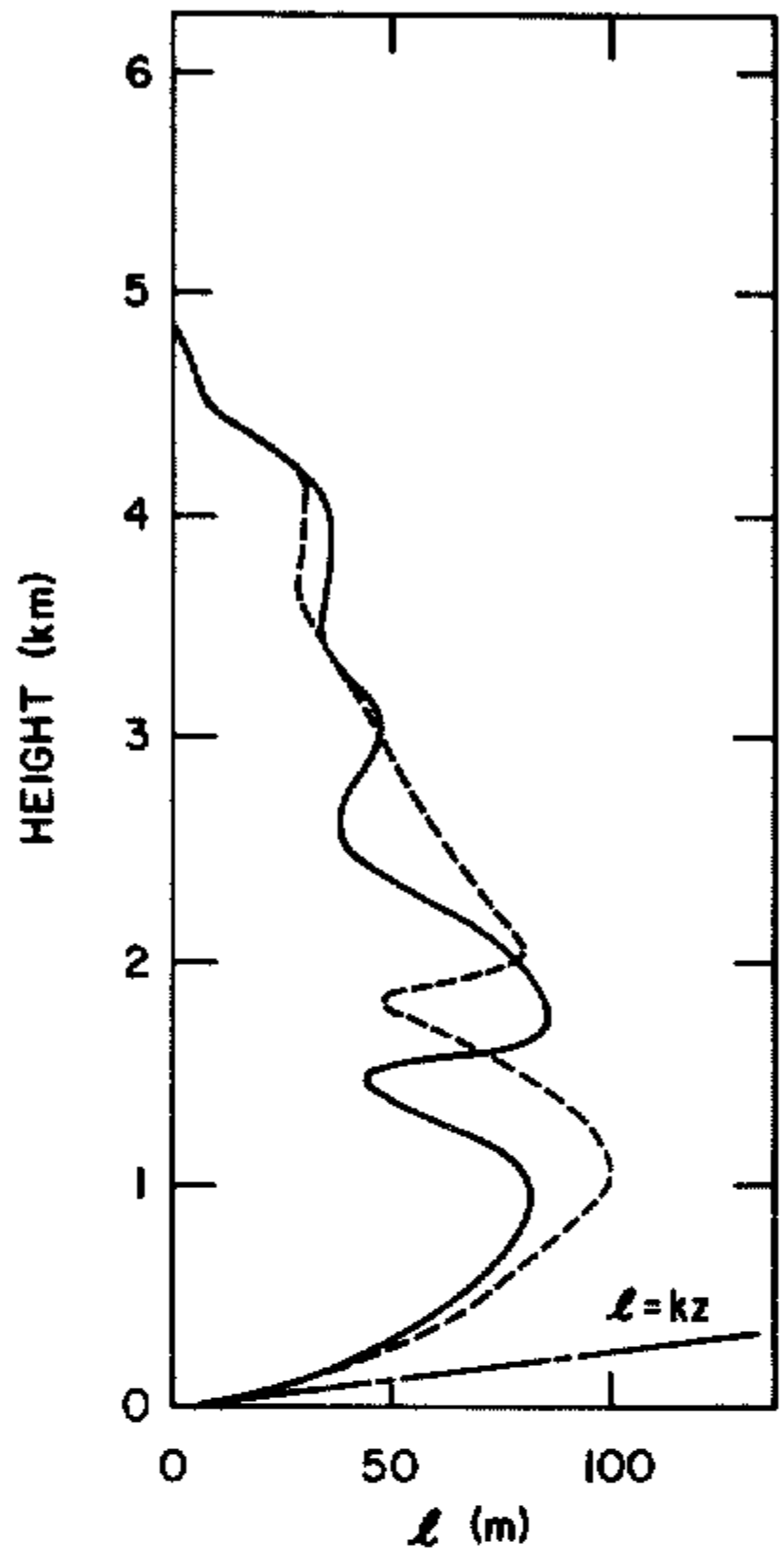

Figure 17. Simulated master length scale at 06 h (continuous) and 15 h (dashes) on 25 June.

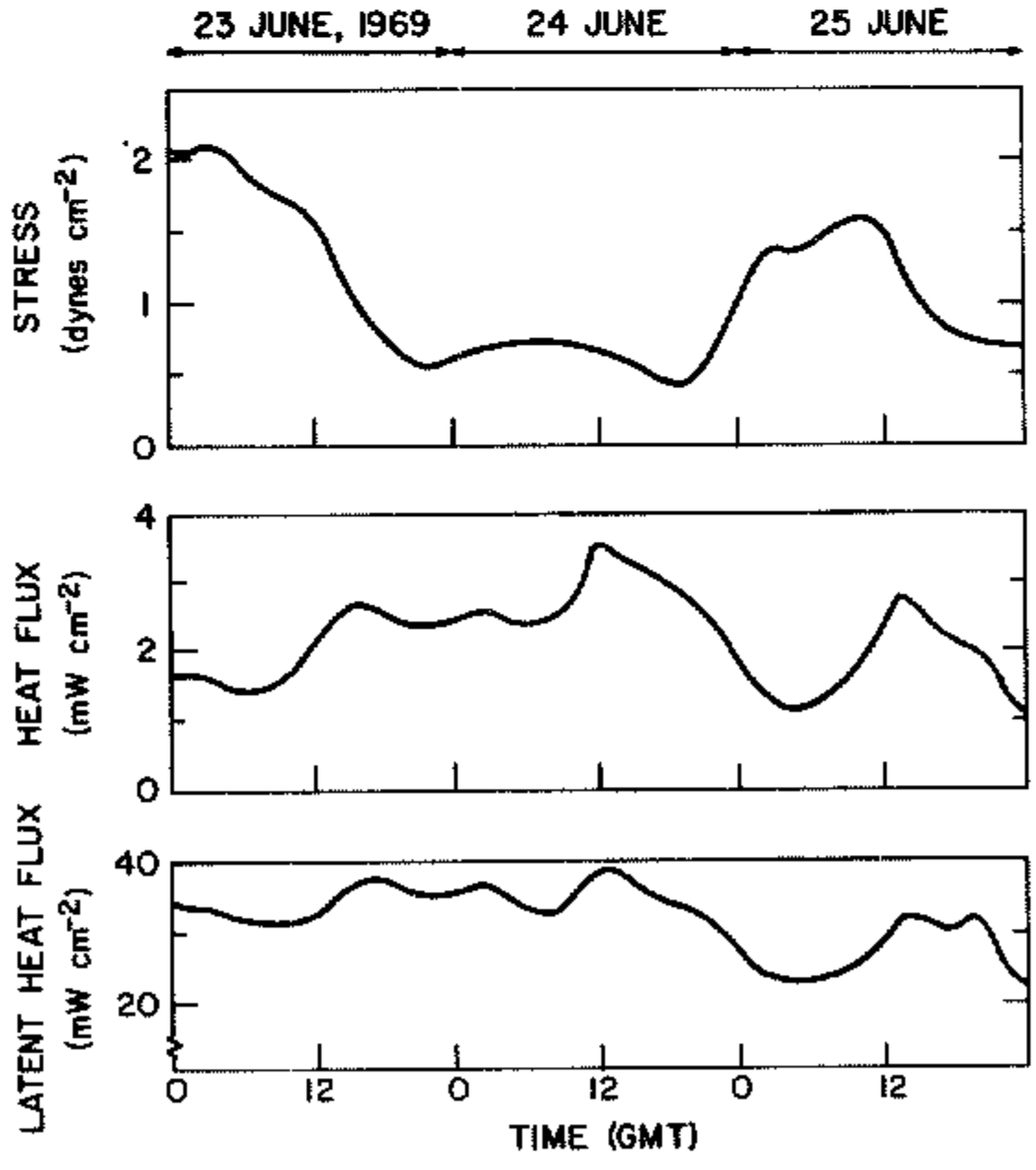

Figure 18. Simulated surface turbulence stress, heat flux and latent heat flux for 23–25 June.

length scale profiles are shown in Figure 17. All these variables indicate penetration much deeper into the upper atmosphere than those for the previous day (Figs. 12, 13, and 14).

The surface turbulence stress, heat flux and latent heat flux are shown in Fig. 18 for 23–25 June. Comparison with corresponding variables observed by Paulson *et al.* (1972) six weeks earlier indicates that the present values are approximately 50% larger than the observations. These differences are mainly due to a surface temperature in the present simulation that is higher than those reported in Paulson *et al.* This appears to be supported by sensitivity tests for the surface temperature variation, as discussed in the following section.

5. Sensitivity tests

Simulated cloud volume is a function of the difference between actual and saturation values of the mixing ratio of water vapour. However, the amount of water vapour is directly influenced by the external driving forces in Eq. (53), i.e., horizontal and vertical advection and the surface boundary condition. The purpose of this section is to study the sensitivity of these driving forces to the simulated water vapour profiles. Results for the 'control run', where all three driving forces are included, have been fully discussed in the previous section. In the following discussion, profiles of simulated water vapour of the 'sensitivity runs', where one of the driving forces is omitted, are compared with the control run. All the results are for midnight on 25 June, four days after the integration is initiated.

Figure 19 shows profiles of simulated water vapour where the horizontal advection terms in Eq. (53) are omitted. The observed water vapour, which is the average of profiles measured at the four ships at the corners of the square array in Fig. 1, is also included for comparison. In Fig. 19 the control run shows better agreement with observations than does

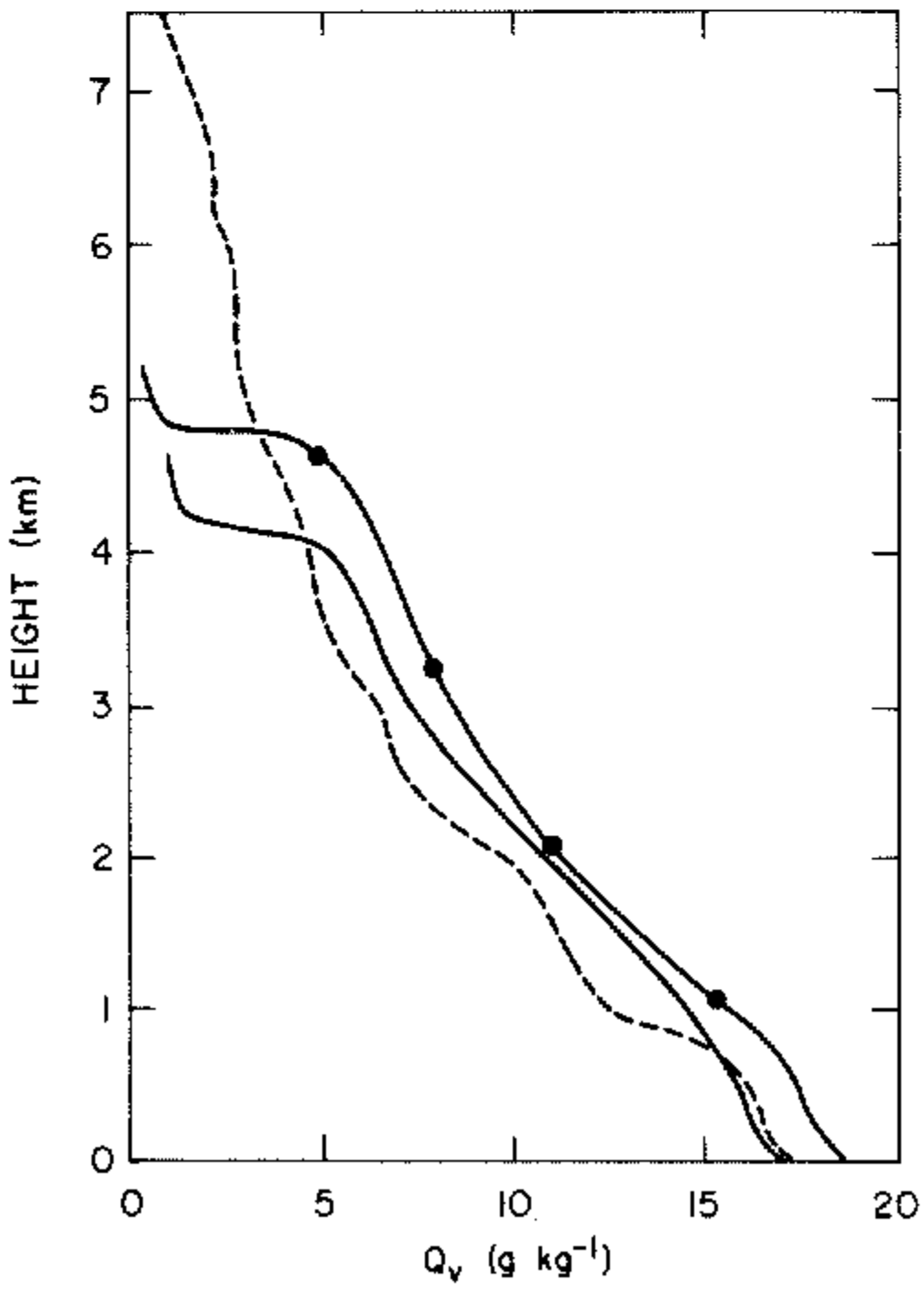

Figure 19. Water vapour at 24 h on 25 June for the control run (continuous) and the sensitivity run (circles) in which the horizontal advection terms in Eq. (53) are omitted. The observed profile is also included (dashed).

the sensitivity run. However, both simulations considerably underestimate water vapour in the layers higher than approximately 5 km above the surface.

Profiles of simulated water vapour, where vertical advection is omitted, are given in Fig. 20. This simulation might be expected to give higher mixing ratios of water vapour than does the control run, since subsidence of the dry upper air is absent in the sensitivity run. This does happen above 1700 m, but not below: water vapour in the first 1700 m of the sensitivity run is lower than in the control run. Closer examination of the results indicates that the air temperature in the inversion layer of the sensitivity run is considerably lower (~4 K) than in the control run, since subsidence is absent in the sensitivity run. A higher mixing ratio of water vapour and a lower saturation mixing ratio, due to the lower temperature in the inversion layer, resulted in more condensation. The latent heat released by condensation produced turbulence that extended as high as 7 km above the surface. Consequently, the water vapour for the sensitivity run is mixed much more uniformly with height, resulting in lower values in the first 1700 m than in the control run.

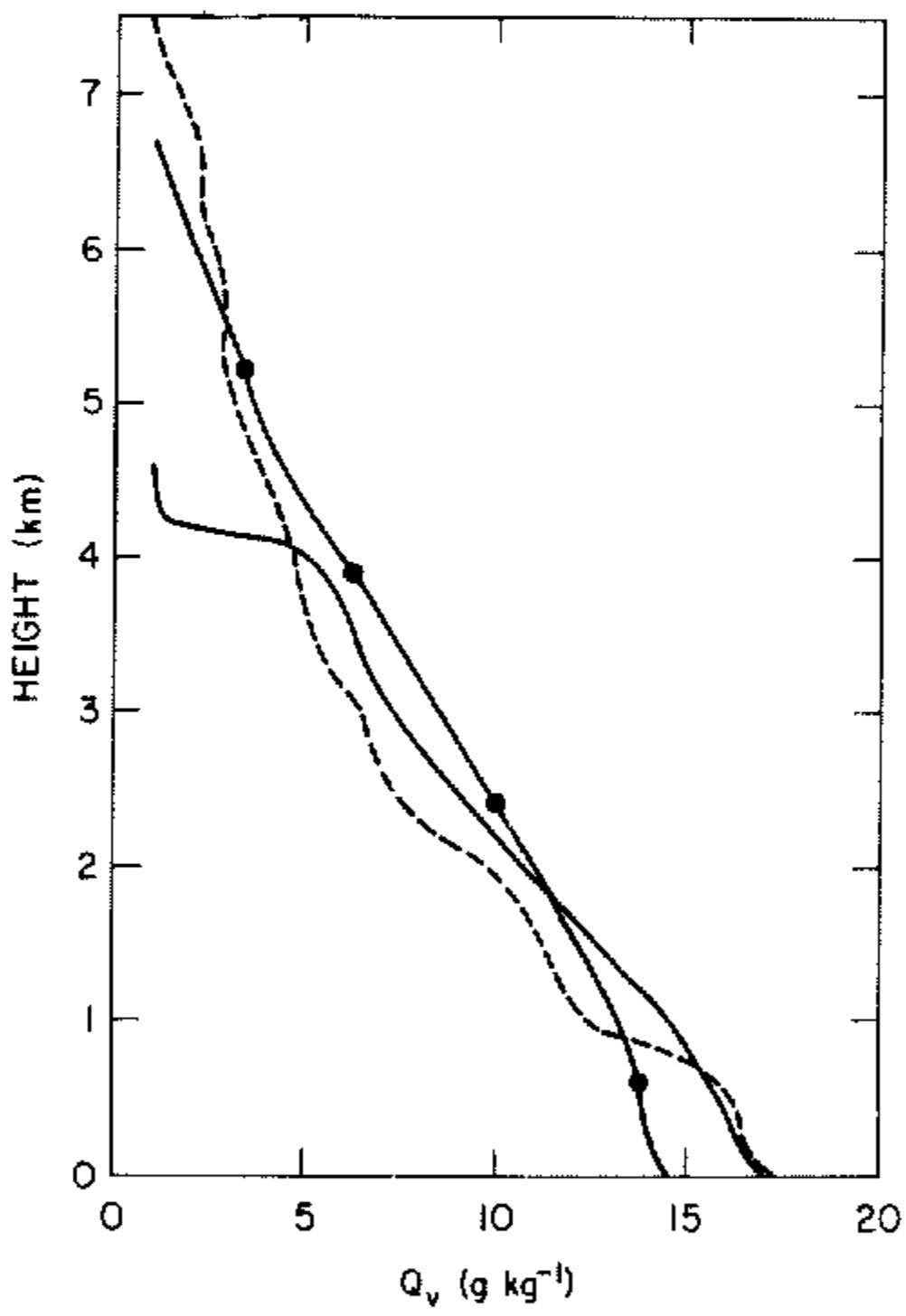

Figure 20. As Fig. 19 except for the sensitivity run, where the vertical advection term in Eq. (53) is omitted.

The surface values of water vapour used in the simulations are determined from the surface temperature by assuming that the air at the surface is saturated. Comparison of the surface temperature used with that observed six weeks earlier (Paulson *et al.* 1972) indicates that the former is about 2 K higher than the latter. Therefore, a final sensitivity test is conducted by lowering the surface temperature by 2 K. Profiles of the simulated water vapour (Fig. 21) show considerable underestimation except in the layer between 1 and 2 km above the surface. However, the surface turbulent fluxes (not shown here) agree much better with the observations reported in Paulson *et al.* than do those from the control run.

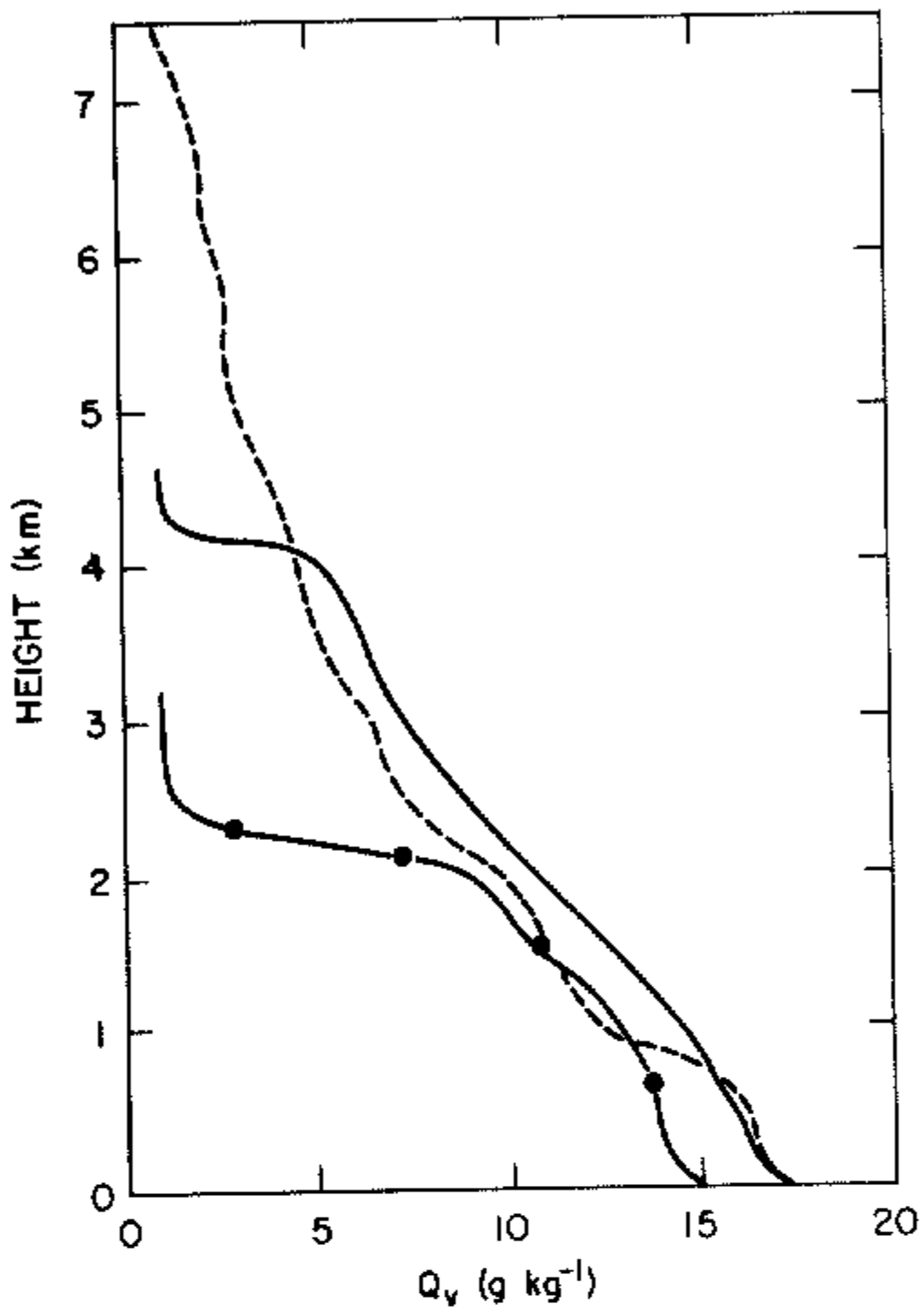

Figure 21. As Fig. 19 except for the sensitivity run, where the surface temperatures are reduced by 2 K.

6. Conclusion

A one-dimensional version of a simplified, second-moment turbulence closure model is used to simulate the BOMEX data. The model solves prognostic equations for horizontal wind components, liquid water potential temperature, mixing ratio of total water, turbulence energy and a master length scale. The somewhat unconventional treatment of condensation and evaporation processes proposed by Sommeria and Deardorff (1977) and Mellor (1977) is used to obtain the mixing ratio of liquid water.

The model is used to simulate the period 22–25 June 1969, when upper air soundings were made and the atmosphere was relatively undisturbed. Simulated horizontal wind speeds in the first 1 km above the surface agree quite well with observations. However, the simulated wind in the upper layer, where turbulent mixing is absent, shows larger vertical shear, mainly due to strong vertical variations of the horizontal pressure gradients used in the present simulation. Simulated temperatures at the end of the period are about 2 K higher than observations in the first 2 km, possibly because the surface temperature used as the boundary condition is too high. Profiles of simulated and observed water vapour also agree reasonably well. Sensitivity studies indicate that the simulated water vapour agrees best with observations when both the vertical wind and the horizontal advection terms obtained from the data are included. Simulated cloud volume is less than 20% on the first day of simulation but increases to as much as 80% on the fourth day. Observed cloud coverage in satellite pictures over the BOMEX area was approximately 30%. Overprediction of cloud volume seems to be a result of the simulated water vapour being slightly higher ($\sim 1{\cdot}5$ g kg^{-1}) than observed, which could be caused either by underestimation of advection or by overestimation of the surface temperature. A sensitivity study indicates that lowering the surface temperature by 2 K decreases the surface latent heat flux by approximately 30%.

The amount of condensation predicted by the present model is a continuous function of the difference between the actual mixing ratio of water vapour and the saturation value. A diagnostic study indicates that if a conventional, instantaneous condensation scheme is used, best agreement with the present simulation is achieved if condensation is assumed to occur at 96% saturation. Simulated turbulence energy and eddy viscosity coefficients obtained from the model are found to increase considerably where condensation occurs. This appears to be reasonable since the latent heat released by condensation produces locally unstable layers.

Acknowledgments

The authors are grateful to Drs J. Shannon and M. Wesely who carefully read the manuscript and made useful suggestions. This work was initiated when T.Y. was at Princeton University where authors benefited from stimulating discussions with scientists at GFDL during the initial stage of the development of the model: we are especially grateful to Dr K. Miyakoda. Work was performed under the auspices of the US Department of Energy (T.Y.) and US Air Force Office of Scientific Research (G.L.M.) under Grant AFOSR 75–2756. The authors are also indebted to Mrs R. Spencer for her excellent typing of the manuscript.

References

André, J. C., DeMoor, G., Lacarrere, P. and du Vachat, R. 1976a Turbulence approximation for inhomogeneous flows – Part I: The clipping approximation, *J. Atmos. Sci.*, **33**, 476–481.

1976b Turbulence approximation for inhomogeneous flows – Part II: The numerical simulation of a penetrative convection experiment, *Ibid.*, **33**, 482–491.

André, J. C., DeMoor, G., Lacarrere, P., Therry, G. and du Vachat, R. 1978 Modeling the 24-hour evolution of the mean and turbulence structures of the planetary boundary layer, *Ibid.*, **35**, 1861–1883.

Betts, A. K. 1973 Non-precipitating cumulus convection and its parameterization, *Quart. J. R. Met. Soc.*, **99**, 178–196.

BOMAP bulletin No. 12 1975 Prepared by Center for Experiment Design and Data Analysis, NOAA, Washington, D.C. 20235.

BOMEX Atlas of Satellite Cloud Photographs 1971 US Dept. of Commerce, NOAA, Environmental Research Laboratories.

Burk, S. D. 1977 The moist boundary layer with a higher-order turbulence closure model, *J. Atmos. Sci.*, **34**, 629–638.

Charnock, H. 1955 Wind stress on a water surface, *Quart. J. R. Met. Soc.*, **81**, 639–640.

Clarke, R. H., Dyer, A. J., Brook, R. R., Reid, D. G. and Troup, A. J. 1971 The Wangara experiment: Boundary layer data, Tech. Paper 19, Div. Met. Phys. CSIRO, Aspendale, Vic. 3195, Australia.

Deardorff, J. W. 1973 The use of subgrid transport equations in a three-dimensional model of atmospheric turbulence. *J. Fluids Eng.*, 429–438.

1974a Three-dimensional numerical study of the height and mean structure of a heated planetary boundary layer, *Boundary-Layer Met.*, **7**, 81–106.

1974b Three-dimensional numerical study of turbulence in an entraining mixed layer, *Ibid.*, **7**, 199–226.

Holland, J. Z. and Rasmusson, E. M. 1973 Measurements of the atmospheric mass, energy, and momentum budgets over a 500-kilometer square of tropical ocean, *Mon. Weath. Rev.*, **101**, 44–55.

Lewellen, W. S. and Teske, M. 1973 Prediction of the Monin-Obukhov similarity functions from an invariant model of turbulence, *J. Atmos. Sci.*, **30**, 1340–1345.

Lewellen, W. S., Teske, M. and Donaldson, C. duP. 1974 Turbulence model of diurnal variations in the planetary boundary layer, Proceeds. *1974 Heat Transfer and Fluid Mechanics Institute*, L. R. Davis and R. E. Wilson, Eds., Standford University Press, 301–319.

Lumley, J. L. and Khajeh-Nouri, E. 1974 Modeling homogeneous deformation of turbulence, *Advances in Geophysics*, **18A**, 162–192.

Mellor, G. L. 1973 Analytic prediction of the properties of stratified planetary surface layers, *J. Atmos. Sci.*, **30**, 1061–1069.

1977 The Gaussian cloud model relations, *Ibid.*, **34**, 356–358; see also Corrigenda, *Ibid.*, **34**, 1483–1484.

Mellor, G. L. and Herring, J. 1973 A survey of the mean turbulent field closure models, *AIAA Journal*, **11**, 590–599.

Mellor, G. L. and Yamada, T. 1974 A hierachy of turbulence closure models for planetary boundary layer, *J. Atmos. Sci.*, **31**, 1791–1806; see also, Corrigenda, *Ibid.*, **34**, 1482.

1977 A turbulence model applied to geophysical fluid problems, Proceedings of a symposium on *Turbulence Shear Flows*, 18–20 April, Penn State Univ., Pennsylvania.

Miyakoda, K. and Sirutis, J. 1977 Comparative integrations of global models with various parameterized processes of subgrid-scale vertical transports: The description of the parameterizations, *Beitr. Phys. Atmos.*, **50**, 445–487.

Nitta, T. and Esbensen, S. 1974 Heat and moisture budget analysis using BOMEX data, *Mon. Weath. Rev.*, **120**, 17–28.

Paulson, C. A., Leavitt, E. and Fleagle, R. G. 1972 Air–sea transfer of momentum, heat and water determined from profile measurements during BOMEX, *J. Phys. Oceanog.*, **2**, 487–497.

Sheppard, P. A. 1958 Transfer across the earth's surface and through the air above, *Quart. J. R. Met. Soc.*, **84**, 205–224.

Sommeria, G. 1976 Three-dimensional simulation of turbulent processes in an undisturbed trade wind boundary layer, *J. Atmos. Sci.*, **33**, 216–241.

Sommeria, G. and Deardorff, J. W. 1977 Subgrid-scale condensation in models of nonprecipitating clouds, *Ibid.*, **34**, 344–355.

Sverdrup, H. U. 1951 Evaporation from the oceans, *Compendium of Meteorology* (edited by J. F. Malone), Waverly Press, Baltimore, MD, USA, 1071–1081.

Wu, J. 1969 Wind stress and surface roughness at air-water interface, *J. Geophys. Res.*, **74**, 444–455.

Wyngaard, J. C. and Coté, O. R. 1974 The evolution of a convective planetary boundary layer – A higher-order closure model study, *Boundary-layer Met.*, **7**, 289–308.

Yamada, T. 1975 The critical Richardson number and the ratio of the eddy transport coefficients obtained from a turbulence closure model, *J. Atmos. Sci.*, **32**, 926–933.

1977 A numerical simulation of pollutant dispersion in a horizontally-homogeneous atmospheric boundary layer, *Atmos. Environ.*, **11**, 1015–1024.

1978 A three-dimensional, second-order closure numerical model of mesoscale circulations in the lower atmosphere, *Topical Report ANL/RER-78-1*, Argonne National Laboratory (available from Argonne National Laboratory).

Yamada, T. and Mellor, G. 1975 A simulation of the Wangara atmospheric boundary layer data, *J. Atmos. Sci.*, **32**, 2309–2329.

Zeman, O. and Lumley, J. L. 1976 Modeling buoyancy driven mixed layers, *Ibid.*, **33**, 1974–1988.

Appendix A

Vertical exchange coefficients

Eliminating $\beta\,\overline{u\theta}_v$ from Eq. (15b) by using Eq. (41), we obtain

$$-\overline{uw} = 3(l_1/q)\{(\overline{w^2}-c_1q^2)(\partial U/\partial z)-g(\beta'_T\overline{u\theta}_l+\beta'_w\overline{uq}_w)\}.$$

Now $u\theta_l$ and $\overline{uq_w}$ may be eliminated from the above expression by use of Eqs. (16a) and (17a). We obtain the following relation after rearrangement:

$$-\overline{uw} = K_M \partial U/\partial z, \quad . \quad . \quad . \quad \text{(A.1)}$$

where
$$K_M = 3l_1\{q(\overline{w^2} - c_1 q^2) + 3l_2 \beta g \overline{w\theta_v}\}/(q^2 + 9l_1 l_2 g \mathscr{S}). \quad . \quad \text{(A.2)}$$

Thus the stress $-\overline{uw}$ is found to be proportional to the wind gradient, $\partial U/\partial z$; and the proportionality constant K_M is given by Eq. (A.2). In a similar fashion we obtain

$$-\overline{vw} = K_M \partial V/\partial z. \quad . \quad . \quad . \quad \text{(A.3)}$$

Now we shall seek a similar expression for $-\overline{w\theta_l}$. Eliminating $\beta\overline{\theta_v\theta_l}$ from Eq. (16c) by using Eq. (43b), we obtain the following expression for $-\overline{w\theta_l}$ after rearrangement:

$$-\overline{w\theta_l} = K_H \partial \Theta_l/\partial z, \quad . \quad . \quad . \quad \text{(A.4)}$$

where
$$K_H = 3l_2(q\overline{w^2} + 0{\cdot}5\Lambda_2 \beta g \overline{w\theta_v})/(q^2 + 1{\cdot}5 l_2 \Lambda_2 g \mathscr{S}). \quad . \quad \text{(A.5)}$$

In a similar fashion we find

$$-\overline{wq}_w = K_H \partial Q_w/\partial z. \quad . \quad . \quad . \quad \text{(A.6)}$$

Thus, fluxes $\overline{uw}$, $\overline{vw}$, $\overline{w\theta_l}$, and $\overline{wq}_w$ are conveniently expressed in terms of eddy viscosity and eddy diffusivity coefficients multiplied by the vertical gradients of the corresponding mean variables. It is surprising to find that such simple relations hold under the rather complex situation presented here. Further algebraic reductions express K_M and K_H in terms of the turbulence energy and mean variables. We note that

$$\beta\overline{w\theta_v} = \beta'_T \overline{w\theta_l} + \beta'_w \overline{wq}_w = -K_H \mathscr{S}, \quad . \quad . \quad \text{(A.7)}$$

where Eqs. (41) and (44) as well as Eqs. (A.4) and (A.6) are used. Substituting Eqs. (A.1), (A.3), and (A.7) into Eq. (14c), we may express $\overline{w^2}$ as

$$\overline{w^2} = q^2/3 + (l_1/q)(-2K_M|\partial \mathbf{V}/\partial z|^2 - 4gK_H \mathscr{S}), \quad . \quad . \quad \text{(A.8)}$$

where
$$|\partial \mathbf{V}/\partial z|^2 = (\partial U/\partial z)^2 + (\partial V/\partial z)^2. \quad . \quad . \quad \text{(A.9)}$$

Substituting Eqs. (A.7) and (A.8) into Eq. (A.2) we obtain the following relation after rearrangement:

$$(q^2 + 6l_1^2|\partial \mathbf{V}/\partial z|^2 + 9l_1 l_2 g \mathscr{S})K_M + 3l_1 g \mathscr{S}(3l_2 + 4l_1)K_H = l_1 q^3(1 - 3c_1). \quad \text{(A.10)}$$

In a similar fashion we may eliminate $\beta\overline{w\theta_v}$ and $\overline{w^2}$ from Eq. (A.5) by using Eqs. (A.7) and (A.8). The resulting equation is

$$6l_1 l_2|\partial \mathbf{V}/\partial z|^2 K_M + \{q^2 + 3l_2 g \mathscr{S}(4l_1 + \Lambda_2)\}K_H = l_2 q^3. \quad . \quad \text{(A.11)}$$

Final expressions for K_M and K_H may be obtained from Eqs. (A.10) and (A.11).

The variance σ_s^2 in Eq. (33) may be conveniently transformed by using the eddy viscosity expressions derived here. The variances $\overline{q_w^2}$ and $\overline{\theta_l^2}$ and the covariance $\overline{q_w\theta_l}$ in Eq. (33) may be eliminated by using Eqs. (18) to (20) after the relations (A.4) and (A.6) are substituted. The resulting expression is

$$\sigma_s^2 = \tfrac{1}{4}(\Lambda_2/q)K_H(a\,\partial Q_w/\partial z - b\,\partial \Theta_l/\partial z)^2. \quad . \quad . \quad \text{(A.12)}$$

Appendix B

List of symbols

a	a parameter defined by Eq. (25a)
A_1, A_2	empirical constants, = 0·92, 0·74
b	a parameter defined by Eq. (25b)
B_1, B_2	empirical constants, = 16·6, 10·1
C_1	empirical constant, = 0·08
e_s	saturation water vapour pressure
E_1, E_2	empirical constants in a length scale equation, = 1·8, 1·33
G	Gaussian probability distribution
l	the master length scale
l_1, l_2, Λ_1, Λ_2	length scales, = $(A_1, A_2, B_1, B_2)l$
P	pressure
P_0	a reference pressure
P_{ij}	mechanical production term in a turbulence energy equation, $\equiv -\overline{u_i w}\,\partial U_j/\partial z$
q^2	twice the turbulence energy, $= \overline{u_i u_i}$
$\overline{q_l^2}$	variance of the mixing ratio of liquid water
q_w	fluctuation of the mixing ratio of total water
Q_v	mixing ratio of water vapour
Q_l	mixing ratio of liquid water
Q_s	saturation mixing ratio
Q_{sl}	saturation mixing ratio at T_l
Q_w	mixing ratio of total water
R	fraction of cloud coverage
R_d	gas constant for dry air
$\tilde{S}_l$	stability function for the eddy viscosity in the length scale equation
$\tilde{S}_q$	stability function for the eddy viscosity in the q^2 equation
$\mathscr{S}$	stability parameter defined by Eq. (44)
T_l	liquid water temperature, $\equiv (P/P_0)^\kappa \Theta_l$
T_0	horizontally averaged temperature
u_*	friction velocity
$\overline{u_k q_w}$	turbulent moisture flux
$\overline{u_k u_j}$	Reynolds stress
$\overline{u_k \theta_l}$	turbulent heat flux
α	molecular diffusivity for Θ_l
β	thermal expansion coefficient, $\approx 1/\Theta_v$
β_T, β_l, β_w	defined by Eqs. (40a), (40b) and (40c), respectively
β'_T, β'_w	defined by Eqs. (42a) and (42b)
ε_{jkl}	alternating tensor
η_w, η_v, η_l	molecular diffusivities for Q_w, Q_v and Q_l, respectively
θ_v	fluctuation of virtual potential temperature
Θ_l	liquid potential temperature, $\equiv \Theta - (\Theta/T)(L_v/c_p)Q_l$
Θ_v	virtual potential temperature, $\equiv \Theta(1 + 0{\cdot}61\,Q_w - 1{\cdot}61\,Q_l)$
κ	ratio R_d/c_p
μ	molecular viscosity
ν	kinematic viscosity
σ_c	condensation rate

σ_r flux divergence of longwave radiation

$\sim$ instantaneous value, except for $\bar{S}_t$ and $\bar{S}_q$

$-$ ensemble average

Other symbols are defined in the text or have their normal meaning.